Evidence that horizontal moisture advection regulates the ubiquitous amplification of rainfall variability over tropical oceans

Kuniaki Inoue*

NASA Goddard Institute for Space Studies, New York, New York,

Universities Space Research Association, Columbia, Maryland,

Lamont-Doherty Earth Observatory, Columbia University, Palisades, New York

Michela Biasutti

Lamont-Doherty Earth Observatory, Columbia University, Palisades, New York

Ann M. Fridlind

NASA Goddard Institute for Space Studies, New York, New York

Corresponding author: Kuniaki Inoue, kuni.inoue22@gmail.com

ABSTRACT

The column moist static energy (MSE) budget equation approximates the processes associated with column moistening and drying in the tropics, and is therefore predictive of precipitation amplification and decay. We use ERA-I and TRMM 3B42 data to investigate day-to-day convective variability and distinguish the roles of horizontal MSE (or moisture) advection versus vertical advection, sources, and sinks. Over tropical convergence zones, results suggest that horizontal moisture advection is a primary driver of day-to-day precipitation fluctuations; when drying via horizontal moisture advection is smaller (greater) than Chikira's "column process," precipitation tends to amplify (decay). In the absence of horizontal moisture advection, precipitation tends to increase spontaneously almost universally through a positive column process feedback. This bulk positive feedback is characterized by negative effective gross moist stability (GMS), which is maintained throughout the tropical convergence zones. How this positive feedback is achieved varies geographically, depending on the shape of vertical velocity (omega) profiles. In regions where omega profiles are top-heavy, the effective GMS is negative primarily owing to strong feedbacks between convection and diabatic MSE sources (radiative and surface fluxes). In these regions, vertical MSE advection stabilizes the atmosphere (positive vertical GMS). Where omega profiles are bottom-heavy, by contrast, a positive feedback is primarily driven by import of MSE through a shallow circulation (negative vertical GMS). The diabatic feedback and vertical GMS are in a see-saw balance, offsetting one another. Our results suggest that ubiquitous convective variability is amplified by the same mechanism as moisture-mode instability.

1. Introduction

a. Background

Atmospheric water vapor is unquestionably of primary importance in weather and climate systems in the deep tropics. Snapshots of column-integrated water vapor (CWV) and precipitation reveal that precipitating convective systems are confined within envelopes of high CWV, and as a filament of high CWV meanders, convective systems within the filament follow the movement of the moisture (e.g., Mapes et al. 2018). This suggests that better understanding of tropical precipitation variability requires better understanding of CWV variability.

One natural way to investigate the processes controlling CWV is to look at the column moisture budget equation. However, two dominant terms in it, vertical moisture advection and precipitation, largely cancel one another, making analysis and interpretation of CWV tendency—a small residual of those dominant terms—difficult. One approach to avoid this inconvenience is to combine all the processes acting in an atmospheric column, namely, vertical moisture advection, precipitation, and surface evaporation, into one "column process" (Chikira 2014). In this way, the CWV tendency is explained by horizontal moisture advection and the column process, which are of a similar magnitude.

Another approach is to investigate the column moist static energy (MSE) budget equation. Because the tendency of column temperature can be taken as negligible in the deep tropics—known as the weak temperature gradient (WTG) approximation (Sobel and Bretherton 2000; Sobel et al. 2001)—the tendency of CWV can be approximated as the tendency of column MSE. Therefore, the column MSE budget equation approximates the processes associated with column moistening and drying.

MSE analysis has been widely exploited in studies of the Madden-Julian Oscillation (MJO; Madden and Julian 1971, 1972). Properties of the MJO such as instability and propagation are explained by considering the MJO as a "moisture mode" (e.g., Sobel et al. 2001; Sobel and Gildor 2003; Raymond and Fuchs 2007; Sugiyama 2009; Sobel and Maloney 2013; Adames and Kim 2016; Fuchs and Raymond 2017), wherein processes that govern large-scale moisture variability also govern precipitation variability. A moisture-mode instability is a positive feedback loop of wet regions getting wetter: a moist atmosphere enhances convection, and enhanced convection in turn moistens the atmosphere, leading to growth of moisture disturbances. Many past studies have examined processes contributing to positive or negative moisture-convection feedbacks in the MJO using the column MSE budget equation (e.g., Maloney 2009; Maloney et al. 2010; Kiranmayi and Maloney 2011; Andersen and Kuang 2011; Hannah and Maloney 2014; Kim et al. 2014; Sobel et al. 2014; Arnold et al. 2015; Inoue and Back 2015a; Yokoi and Sobel 2015; Wolding and Maloney 2015; Benedict et al. 2020).

Column radiative heating contributes to a positive moisture-convection feedback in the MJO; in an enhanced phase of the MJO, anomalous radiative heating associated with deep clouds creates positive temperature anomalies in the free troposphere, which are rapidly converted into anomalous large-scale ascent (e.g., Bretherton and Smolarkiewicz 1989; Sobel and Bretherton 2000; Sobel et al. 2001). Such large-scale ascent augments the existing convection, and also transports moisture vertically, moistening the free troposphere (e.g., Chikira 2014; Wolding and Maloney 2015; Janiga and Zhang 2016; Wolding et al. 2016; Adames 2017), which creates a more favorable environment for further convection. Surface fluxes (especially surface evaporation) may also contribute to a positive feedback through enhanced surface wind speeds in a mature phase of the MJO (e.g., Araligidad and Maloney 2008; Maloney 2009; Maloney et al. 2010; Kiranmayi and Maloney 2011;

Kim et al. 2014; Sobel et al. 2014; Dellaripa and Maloney 2015; Arnold et al. 2015; Inoue and Back 2015a; Yokoi and Sobel 2015; Wolding and Maloney 2015).

On the other hand, horizontal and vertical MSE advection tend to contribute to a negative feedback in the MJO, counteracting the moistening processes due to radiation and surface fluxes (e.g., Maloney 2009; Maloney et al. 2010; Kiranmayi and Maloney 2011; Andersen and Kuang 2011; Kim et al. 2014; Sobel et al. 2014; Arnold et al. 2015; Inoue and Back 2015a; Yokoi and Sobel 2015; Wolding and Maloney 2015). Furthermore, vertical MSE advection and column radiative heating are not independent of one another, but some fraction of vertical MSE advection is due to the radiatively driven large-scale motions (e.g., Chikira 2014; Wolding and Maloney 2015; Janiga and Zhang 2016; Wolding et al. 2016; Adames 2017). Therefore, it may be beneficial to consider vertical MSE advection and column radative heating together.

When the positive MSE feedbacks due to radiation and surface fluxes exceed the negative effects due to total MSE advection, the MJO may be destabilized. This general instability mechanism can be considered as a core aspect of the moisture-mode theoretical framework, common to all of the moisture-mode studies cited above.

This instability mechanism also explains amplification and decay of more general convective variability, not limited to the MJO (e.g., Masunaga and L'Ecuyer 2014; Inoue and Back 2015b, 2017). For instance, Inoue and Back (2017) (hereafter, IB17) applied the above instability mechanism to ubiquitous convective variability[1], and found that it explains day-to-day precipitation amplification and decay over tropical oceanic regions. This instability framework has been also proven to be useful to assess the onset of the South Asian Summer Monsoon (e.g., Ma et al. 2019).

[1]In this study, the term "ubiquitous convective variability" designates random convective variability, not regulated by any specific mode such as the MJO or convectively coupled equatorial waves.

Due to data constraints, IB17 did not address the different roles of horizontal and vertical MSE advection in the moisture-convection feedback. Horizontal and vertical MSE advection are linked to convective variability in different ways. Variability in vertical MSE advection is primarily determined by variability in the shape and amplitude of the vertical velocity (ω) profiles rather than variability in the MSE profiles on which ω operates. An ω profile tends to evolve from a bottom-heavy into a top-heavy shape as a convective system develops (e.g., Mapes et al. 2006; Inoue and Back 2015a; Fuchs-Stone et al. 2020). A bottom-heavy ω profile is associated with the import of MSE through a lower-tropospheric shallow circulation whereas a top-heavy profile exports MSE through a deep circulation [see Fig. 1 in Inoue and Back (2015b)]. At the same time, the amplitude of ω determines the amplitude of the import or export. By contrast, horizontal MSE advection is dependent on nonlocal factors such as the horizontal gradient of moisture, and the direction and intensity of rotational winds.

Furthermore, the shape of climatological ω profiles varies geographically. Specifically, the climatological ω profile is bottom-heavy over the eastern Pacific and Atlantic Oceans whereas it is top-heavy over the western Pacific and Indian Oceans (e.g., Back and Bretherton 2006, 2009; Back et al. 2017; Inoue et al. 2020). Thus, it can be inferred that climatological behaviors of vertical MSE advection also vary geographically.

This study seeks to answer the following questions:

1. What roles do horizontal and vertical MSE advection play in controlling day-to-day convective variability?

2. How do those roles differ geographically?

To systematically address these questions, we derive a parsimonious expression of convective variability by simplifying the framework that IB17 applied to daily variability over tropical convergence zones. In the next subsection, we briefly summarize IB17.

b. Summary of IB17

The basis of IB17 is the column dry static energy (DSE) and moisture budget equations (expressed in energy units) in pressure coordinates:

$$\frac{\partial \langle s \rangle}{\partial t} = -\nabla \cdot \langle s\mathbf{v} \rangle + LP + \langle Q_R \rangle + H \,, \text{ and} \tag{1}$$

$$\frac{\partial \langle Lq \rangle}{\partial t} = -\nabla \cdot \langle Lq\mathbf{v} \rangle + LE - LP \,, \tag{2}$$

where $s \equiv c_p T + gz$ is dry static energy (DSE); $c_p T$ is enthalpy; gz is geo-potential; $\mathbf{v}$ is horizontal wind velocity; ∇ is the isobaric horizontal gradient operator; P is precipitation; L is the latent heat of vaporization; Q_R is radiative heating; H is a surface sensible heat flux; q is specific humidity; E is surface evaporation. The angle brackets are defined as

$$\langle \ \rangle \equiv \frac{1}{g} \int_{p_t}^{p_s} \mathrm{d}p \,, \tag{3}$$

where p_t is the tropopause pressure, which is assumed to be 100 hPa, and p_s is the surface pressure. Following Johnson and Ciesielski (2000), hydrometeor storage effects are neglected in Eqs. (1) and (2).

Adding Eq. (1) to Eq. (2) yields the column MSE budget equation:

$$\frac{\partial \langle h \rangle}{\partial t} = -\nabla \cdot \langle h\mathbf{v} \rangle + D \,, \tag{4}$$

where $h \equiv s + Lq$ is MSE. The diabatic source term, D, has been defined as

$$D \equiv \langle Q_R \rangle + LE + H \,. \tag{5}$$

Here we use MSE instead of frozen MSE for simplicity without loss of generality; for instance, Fridlind et al. (2012) found that analyses of column budgets from cloud-resolving simulations of tropical convection were negligibly affected by that choice. Since MSE is approximately conserved in adiabatic displacements, it is a useful quantity for studying precipitating convective systems.

Equation (4) is converted into a "precipitation equation" via three empirical relationships. First, we make the WTG approximation (i.e., $\partial\langle s\rangle/\partial t \simeq 0$) (Sobel and Bretherton 2000; Sobel et al. 2001), removing the DSE tendency from Eq. (4). The WTG approximation is most often assumed on intraseasonal or longer timescales, but Inoue and Back (2015b) showed that it can also be a reasonable approximation over day-to-day variability if the diurnal cycle is removed.

Second, Bretherton et al. (2004) found that precipitation can be expressed as an exponential function of column-integrated water vapor (CWV; or precipitable water). Thus, we can express precipitation tendency as

$$\frac{\partial \ln P}{\partial t} \propto \frac{\partial \langle q\rangle}{\partial t}\,, \tag{6}$$

where $\propto$ represents proportionality, as confirmed in Appendix A.

Third, we assume empirical relationships between radiation, surface fluxes, and convection. In the tropical convergence zones, column-integrated radiative heating is positively correlated with convective intensity (e.g., Su and Neelin 2002; Bretherton and Sobel 2002; Lin and Mapes 2004; Peters and Bretherton 2005; Kiranmayi and Maloney 2011; Sobel et al. 2014; Kim et al. 2014; Inoue and Back 2015a,b; Yokoi and Sobel 2015; Wolding and Maloney 2015, and many GCM studies). Additionally, there exists a positive correlation between surface fluxes and convective intensity (e.g., Raymond et al. 2003; Back and Bretherton 2005; Raymond et al. 2006; Maloney and Esbensen 2007; Araligidad and Maloney 2008; Kiranmayi and Maloney 2011; Kim et al. 2014; Sobel et al. 2014; Dellaripa and Maloney 2015; Inoue and Back 2015a,b; Yokoi and Sobel 2015; Wolding and Maloney 2015, and many GCM studies), which may be due to downdraft-induced

enhancements of gustiness (e.g., Redelsperger et al. 2000) or boundary-layer quasi-equilibrium (Raymond 1995). Inoue and Back (2015b) and IB17 posited that these relationships between radiation, surface fluxes, and convection, can be succinctly expressed as

$$D \simeq \widetilde{\gamma} \nabla \cdot \langle s\mathbf{v} \rangle \tag{7}$$

where $\widetilde{\gamma}$ represents the sum of cloud-radiation and convection-surface-flux feedbacks, which is determined by the background environment. The tilde indicates that the parameter is assumed invariant on sub-seasonal timescales and only varies geographically and seasonally. As $\nabla \cdot \langle s\mathbf{v} \rangle$ is a good proxy for precipitation, here it is representative of convective intensity. The validity of this relationship was discussed in depth in Inoue and Back (2015b) and IB17. Here it is sufficient to say that this proportionality holds over most of the convective regions, although not in the central Pacific, where D remains negligible, regardless of the intensity of convection (as will be shown in Section 3b).

Applying the WTG approximation and Eqs. (6)–(7) to Eq. (4) yields

$$\frac{\partial \ln P}{\partial t} \propto -\nabla \cdot \langle h\mathbf{v} \rangle + \widetilde{\gamma} \nabla \cdot \langle s\mathbf{v} \rangle \ . \tag{8}$$

This equation indicates that the balance between $\nabla \cdot \langle h\mathbf{v} \rangle$ and $\widetilde{\gamma} \nabla \cdot \langle s\mathbf{v} \rangle$ is predictive of whether precipitation will amplify or decay in the following day. Where $\widetilde{\gamma}$ becomes zero, precipitation variability is solely determined by $\nabla \cdot \langle h\mathbf{v} \rangle$.

This result is closely related to a theoretical quantity referred to as gross moist stability (GMS) (e.g., Neelin and Held 1987; Raymond et al. 2009). If GMS is defined as

$$\Gamma \equiv \frac{\nabla \cdot \langle h\mathbf{v} \rangle}{\nabla \cdot \langle s\mathbf{v} \rangle} \, , \tag{9}$$

then Eq. (8) indicates that the balance between the GMS (temporally variant) and $\widetilde{\gamma}$ (temporally invariant) is predictive of whether precipitation will amplify or decay on a daily timescale. Inoue

and Back (2015b) and IB17 referred to $\widetilde{\gamma}$ as the characteristic or critical GMS because it defines a threshold delineating the amplification versus decay of convective systems statistically.

Although IB17 showed that Eq. (8) represents the statistics of convective variability adequately, this equation can be further decomposed into the contributions of horizontal and vertical advective terms. By assuming ω to be negligible at $p = p_s, p_t$, and taking an integration by parts, the column-integrated flux divergence of MSE can be decomposed as[2] (e.g., Raymond et al. 2009)

$$\nabla \cdot \langle h\mathbf{v} \rangle = \langle \mathbf{v} \cdot \nabla h \rangle + \left\langle \omega \frac{\partial h}{\partial p} \right\rangle , \tag{10}$$

and similarly for the DSE and moisture advection. We accordingly decompose Eq. (8) into the contributions of horizontal and vertical advection, and assess their different roles in convective variability.

2. Methods

a. Data

1) ERA-INTERIM

We use T, z, $\mathbf{v}$, ω, q, and p_s from the European Centre for Medium-Range Weather Forecasts (ECMWF) Reanalysis-interim (ERA-interim, hereafter ERA-I; Dee et al. 2011) with a 6-hourly and ~0.7°×0.7° resolution. First, we regrid each variable onto a daily and ~1.4°×1.4° resolution by taking a temporal and spatial average. We then compute the column-integrated tendencies and the horizontal and vertical advective terms for DSE, specific humidity, and MSE. This procedure neglects sub-grid and sub-daily covariance in the advection terms[3].

[2]The horizontal gradient of p_s was also ignored for ∇ and $\langle\ \rangle$ to commute.

[3]The sub-grid and sub-daily covariance of moisture advection is negligible on monthly mean in the deep tropics (e.g., Seager and Henderson 2013). We assume that is also the case on a daily timescale.

2) TRMM 3B42

Precipitation data are obtained from version 7 of the daily TRMM Multisatellite Precipitation Analysis (TMPA) known as the TRMM 3B42 product (Huffman et al. 2007, 2010). The raw data with a daily and 0.25°×0.25° resolution are regridded onto the same grid as that for ERA-I, using first-order conserved remapping (Jones 1999).

b. Estimation of the diabatic source

We estimate the MSE diabatic source term as a residual of Eq. (4), or

$$D = \frac{\partial \langle h \rangle}{\partial t} + \nabla \cdot \langle h\mathbf{v} \rangle \ , \tag{11}$$

instead of using ERA-I radiation and surface fluxes. We chose this method because the MSE budget is not closed if the predicted fluxes are used (e.g., Kim et al. 2014; Yasunaga et al. 2019), and h and $\mathbf{v}$ may be more constrained by data assimilation. Issues with this estimate are discussed in Section 4d. We use the values of D solely to compute $\widetilde{\gamma}$ from Eq. (7) in each grid box, by regression of D against $\nabla \cdot \langle s\mathbf{v} \rangle$ through the origin. Our primary interest is the geographic pattern of $\widetilde{\gamma}$ (shown in Fig. 5), which compares reasonably well with Fig. 9 in IB17 computed from satellite observations.

c. Time period and spatial domains

We analyze June-July-August (JJA) and December-January-February (DJF) data from 1998 to 2012. All figures show results for JJA, which are in general representative of both seasons, unless otherwise specified. Since our primary interest is convectively active regions or convergence zones, we focus our analysis on areas where the mean value of $\langle \omega \partial s / \partial p \rangle$ exceeds 50 W/m^2 (enclosed by the gray line in Fig. 1). Furthermore, following Inoue and Back (2017), detailed analyses are

conducted over four oceanic regions: the Indian Ocean (IO), western Pacific (WP), central Pacific (CP), and Atlantic Ocean (AO), designated with the green boxes in Fig. 1. The regions are selected such that each contains the same number of grid points.

d. Top-heaviness ratio

The shape of ω profiles is crucial for vertical MSE advection. To characterize the shape, we utilize the top-heaviness ratio (e.g., Back et al. 2017; Inoue et al. 2020), computed as follows. We approximate ω profiles with two leading components,

$$\omega(x,y,p,t) \simeq o_1(x,y,t)\Omega_1(p) + o_2(x,y,t)\Omega_2(p)\,, \tag{12}$$

where Ω_1 and Ω_2 are respectively the first and second empirical orthogonal functions (EOFs) depicted in Fig. 2(a), designated EOF1 and EOF2; o_1 and o_2 represent the corresponding principal components. Before computing the EOFs, we zero out the artificial values of ω below the surface pressure, which are products of extrapolation from model to pressure coordinates. The EOFs are then computed over the tropical convergence zones enclosed by the gray line in Fig. 1.

The top-heaviness ratio, τ, is defined as

$$o_2 \equiv \tau o_1\ . \tag{13}$$

We estimate τ for each location, following Inoue et al. (2020), as

$$\widetilde{\tau}(x,y) = \frac{\overline{o_1' \times o_2'}}{\overline{o_1'^2}} \tag{14}$$

where the bar represents a time average and the prime represents a temporal anomaly. Figure 2(b) illustrates the shape of ω profiles as a function of $\widetilde{\tau}$ (see Section 3e).

3. Results

We begin by verifying Eq. (8) using the data sets described above. We then compare the geographic pattern of $\widetilde{\gamma}$ with that obtained by IB17 using satellite observations. Finally, we separate total MSE advection into horizontal and vertical components, and examine their different roles in convective variability to answer the questions posed in Section 1a.

a. GMS plane analysis

Equation (8) is examined in Fig. 3, which shows the probability of precipitation being amplified in the next day as a function of $\nabla \cdot \langle h\mathbf{v} \rangle$ and $\nabla \cdot \langle s\mathbf{v} \rangle$. To calculate the probability, we first compare each day's precipitation with the following day's precipitation to identify whether precipitation increases or decreases. We then sort all days into bins according to their values of $\nabla \cdot \langle h\mathbf{v} \rangle$ and $\nabla \cdot \langle s\mathbf{v} \rangle$. Finally, we compute the ratio of the number of days with amplified precipitation to the number of total days within each bin. The red shades indicate that precipitation tends to amplify in the following day with a probability exceeding 60%, whereas the blue colors indicate a probability of amplification less than 40%, meaning that precipitation will more likely decay. The bin size is determined based on the distributions of $\nabla \cdot \langle h\mathbf{v} \rangle$ and $\nabla \cdot \langle s\mathbf{v} \rangle$ in each oceanic basin[4], and the results are insensitive to the details of bin-size choice. The dashed-line slopes correspond to $\widetilde{\gamma}$ in Eq. (7), calculated with regression through the origin over each oceanic basin. It should be noted that this probability metric is independent of the amplitude of precipitation changes so that the results are not biased by large variability events.

Figure 3 shows that the grid points below the $\widetilde{\gamma}$-line—corresponding to a positive RHS of Eq. (8)—have a high probability of precipitation amplification. By contrast, the grid points above

[4]The bin size for $\nabla \cdot \langle h\mathbf{v} \rangle$ is equal to the 95-percentile minus the 5-percentile of $\nabla \cdot \langle h\mathbf{v} \rangle$ (see Fig. 6) divided by 10, and the bin size for $\nabla \cdot \langle s\mathbf{v} \rangle$ is equal to the 95-percentile minus the 5-percentile of $\nabla \cdot \langle s\mathbf{v} \rangle$ divided by 20.

the $\widetilde{\gamma}$-line—corresponding to a negative RHS of Eq. (8)—have a high probability of decaying precipitation. We replicated this figure for DJF, and found no notable differences (not shown) except for the dashed-line slopes or $\widetilde{\gamma}$ values, which are shown in Section 3e. This result confirms that Eq. (8) predicts the amplification or decay of precipitation statistically. Since $\nabla \cdot \langle h\mathbf{v} \rangle$ and $\nabla \cdot \langle s\mathbf{v} \rangle$ are the numerator and denominator of Γ, respectively, IB17 denote a plane defined by those axes as the "GMS plane." The grid points near the $\widetilde{\gamma}$-line correspond to $\partial P / \partial t \simeq 0$, following Eq. (8). Their precipitation changes are thus small, which can explain why those grid points exhibit weak predictive skill (depicted by the gray color). The metric of amplification probability is also most sensitive around the $\widetilde{\gamma}$-line to small errors in the data used and in the derived theory itself.

Figure 4 shows the joint distributions of $\nabla \cdot \langle h\mathbf{v} \rangle$ and $\nabla \cdot \langle s\mathbf{v} \rangle$ using the same bins as in Fig. 3. Over each oceanic basin, the peak of the distribution (orange cross symbol) is located near the $\widetilde{\gamma}$-line. Furthermore, the ridge of the joint PDF approximately follows the $\widetilde{\gamma}$-line. This indicates that atmospheric columns are commonly close to the balanced condition of $\nabla \cdot \langle h\mathbf{v} \rangle = \widetilde{\gamma} \nabla \cdot \langle s\mathbf{v} \rangle$ (i.e., $\partial \langle Lq \rangle / \partial t \simeq 0$) where convection is in a quasi-steady state with small day-to-day precipitation changes. When an atmospheric column is close to this condition, its location on the GMS plane is not predictive of precipitation amplification or decay. Since the distributions of $\nabla \cdot \langle h\mathbf{v} \rangle$ and $\nabla \cdot \langle s\mathbf{v} \rangle$ are generally concentrated around this condition, the gray areas in Fig. 3 account for 40%, 41%, 35%, and 39% of the total data points over the Indian Ocean, western Pacific, central Pacific, and Atlantic Ocean basins, respectively. But as an atmospheric column departs further from this balanced condition (i.e., away from the $\widetilde{\gamma}$-line), its location on the GMS plane is increasingly predictive of precipitation amplification or decay.

Figures 3 and 4 offer a conceptual understanding of tropical convective variability in general. Namely, for large-scale ensembles of convection, day-to-day variability of precipitation is correlated with departures of the environment from the balanced condition of $\nabla \cdot \langle h\mathbf{v} \rangle = \widetilde{\gamma} \nabla \cdot \langle s\mathbf{v} \rangle$. When

this balance is achieved, the atmosphere may exhibit a quasi-steady state in which the convective intensity becomes steady, as in an aggregated convective system in radiative convective equilibrium simulations (e.g., Wing et al. 2017). When advection perturbs this balanced condition, ensemble-mean precipitation amplifies or decays, depending on the balance between $\nabla \cdot \langle h\mathbf{v} \rangle$ and $\widetilde{\gamma} \nabla \cdot \langle s\mathbf{v} \rangle$.

b. Geographic variability of $\widetilde{\gamma}$

Figure 5 shows the geographical pattern of $\widetilde{\gamma}$ for JJA. The result for DJF is discussed in Section 3e. High values of $\widetilde{\gamma}$ indicate strong positive feedbacks between convection and the diabatic source term (radiation plus surface fluxes). The Indian Ocean and western Pacific exhibit high values of $\widetilde{\gamma}$ whereas the central Pacific has the lowest values, which are close to zero and slightly negative. The Atlantic Ocean also exhibits lower values than the Indian Ocean and western Pacific. These patterns are largely consistent with IB17, but the values of $\widetilde{\gamma}$ in this study are considerably higher than theirs and more comparable to those computed with the field campaign data (see Table A1 in IB17). The discrepancy with IB17 could be attributable to the underestimation of the cloud-radiation feedback in the satellite data used by IB17 (as discussed in IB17's Appendix).

Some patterns not described in IB17 are worth noting. The Mesoamerican region, especially the Caribbean Sea, has high values of $\widetilde{\gamma}$. The South Pacific Convergence Zone (SPCZ; ~0°–15°S in the western Pacific) exhibits lower values compared to the northwestern Pacific, resulting in a clear contrast between the northern and southern parts of the western Pacific. Africa exhibits high values, especially around the Congo Basin. The Amazon Basin exhibits slightly higher $\widetilde{\gamma}$ values than the Atlantic Ocean, but not as high as Africa.

However, the fidelity of $\widetilde{\gamma}$ is questionable over land. The sensible heat flux, which is negligible over the tropical oceans (e.g., Yu and Weller 2007), is expected to be non-negligible over land. The contributions of evapotranspiration to the moisture budget also need to be included there. Thus,

it is uncertain that Eq. (7) holds over land. Furthermore, due to the lack of observational surface flux data with high resolution and wide spatial coverage over land, the assessment of $\widetilde{\gamma}$ there has big uncertainties. Therefore, continental patterns of $\widetilde{\gamma}$ and their physical interpretation require additional investigation with other independent data sets.

c. Variability of horizontal and vertical MSE advection

Figure 6 shows the distributions of total MSE advection ($\nabla \cdot \langle h\mathbf{v} \rangle$, orange), and its horizontal ($\langle \mathbf{v} \cdot \nabla h \rangle$, blue), and vertical ($\langle \omega \partial h/\partial p \rangle$, green) components over each oceanic basin. The diamonds on the top axis represent the mean values, and the triangles on the bottom axis represent the 5- and 95-percentiles of each advective term in the same colors. Means and variances of each advective term are summarized in Table 1.

There are some discernible differences in the distributions of $\langle \omega \partial h/\partial p \rangle$ among the different oceanic basins. First, the signs of the mean values, $\overline{\langle \omega \partial h/\partial p \rangle}$, differ (Table 1). Over the warm pool region (the Indian Ocean and western Pacific), the means are positive, indicating that the vertical advection climatologically exports MSE through a deep circulation. By contrast, they are negative over the central Pacific and Atlantic Ocean, indicating that the vertical advection climatologically imports MSE through a shallow circulation. This is consistent with Back and Bretherton (2006). Furthermore, over the central Pacific and Atlantic Ocean, positive $\overline{\langle \mathbf{v} \cdot \nabla h \rangle}$ is offset by negative $\overline{\langle \omega \partial h/\partial p \rangle}$, resulting in small values of $\overline{\nabla \cdot \langle h\mathbf{v} \rangle}$. By contrast, in the warm pool region, both $\overline{\langle \mathbf{v} \cdot \nabla h \rangle}$ and $\overline{\langle \omega \partial h/\partial p \rangle}$ are positive and additive. In short, MSE over the warm pool region is climatologically exported via both horizontal and vertical advection whereas the total advection over the central Pacific and Atlantic Ocean is small due to the cancellation between the horizontal and vertical advection.

Second, the distributions of $\langle \omega \partial h/\partial p \rangle$ are narrower over the central Pacific and Atlantic Ocean, compared to those over the Indian Ocean and western Pacific. The vertical MSE advection therefore contributes less to the variability of the total MSE advection over the central Pacific and Atlantic Ocean than over the warm pool region.

Despite those differences, a consistent pattern among the different basins emerges in Fig. 6: the distributions of $\langle \mathbf{v} \cdot \nabla h \rangle$ are much wider than those of $\langle \omega \partial h/\partial p \rangle$ over all the basins. The covariance between $\langle \mathbf{v} \cdot \nabla h \rangle$ and $\langle \omega \partial h/\partial p \rangle$ is negligible, and the variance of $\nabla \cdot \langle h\mathbf{v} \rangle$ is largely explained by that of $\langle \mathbf{v} \cdot \nabla h \rangle$ (Table 1). Therefore, the variability of the total MSE advection is predominantly explained by the variability of the horizontal MSE advection. This result suggests that the horizontal MSE (or moisture) advection plays a dominant role in MSE variability over the tropical oceanic regions.

d. Primary driver of precipitation variability

Here, we investigate the different roles of horizontal and vertical MSE advection in precipitation variability. Vertical MSE advection can be viewed as a feedback process in which deep convection exports more MSE, reducing column MSE (damping), and shallow convection does the opposite (amplifying). In this view, vertical MSE advection is a function of convective intensity and feedback efficiency, which can be expressed as the vertical component of the GMS. Namely, the GMS can be decomposed as

$$\Gamma \equiv \frac{\nabla \cdot \langle h\mathbf{v} \rangle}{\nabla \cdot \langle s\mathbf{v} \rangle} \tag{15}$$

$$= \frac{\langle \mathbf{v} \cdot \nabla h \rangle}{\nabla \cdot \langle s\mathbf{v} \rangle} + \frac{\left\langle \omega \frac{\partial h}{\partial p} \right\rangle}{\nabla \cdot \langle s\mathbf{v} \rangle} \, . \tag{16}$$

If the horizontal DSE gradient is neglected (e.g., Sobel and Bretherton 2000; Sobel et al. 2001),

$$\Gamma \simeq \frac{\langle \mathbf{v} \cdot \nabla Lq \rangle}{\left\langle \omega \frac{\partial s}{\partial p} \right\rangle} + \frac{\left\langle \omega \frac{\partial h}{\partial p} \right\rangle}{\left\langle \omega \frac{\partial s}{\partial p} \right\rangle} \tag{17}$$

$$\equiv \Gamma_{\mathrm{h}} + \Gamma_{\mathrm{v}} \,, \tag{18}$$

where Γ_{h} and Γ_{v} have been referred to as the horizontal and vertical GMS, respectively (e.g., Raymond et al. 2009).

Precisely speaking, the vertical GMS varies in time, for instance when following a convective system as it evolves from a shallow to deep circulation (e.g., Inoue and Back 2015b). However, this study assumes it to be locally constant, ignoring temporal variations in the shape of ω profiles. Why and when this assumption becomes valid is discussed later in this subsection.

When assuming the vertical GMS to be a constant, vertical MSE advection can be considered as a simple linear feedback process whose feedback efficiency is constant vertical GMS. However, because the shape of climatological ω profiles varies geographically (e.g., Back and Bretherton 2006, 2009; Back et al. 2017; Inoue et al. 2020) and seasonally (Section 3e), here we also assume that the vertical GMS varies geographically and seasonally. Thus, vertical MSE advection can be expressed as

$$\left\langle \omega \frac{\partial h}{\partial p} \right\rangle = \widetilde{\Gamma}_{\mathrm{v}} \left\langle \omega \frac{\partial s}{\partial p} \right\rangle \,, \tag{19}$$

where $\langle \omega \partial s / \partial p \rangle$ represents the intensity of convection, and the tilde indicates that the parameter is considered temporally invariant at subseasonal timescales, as discussed in Section 3e.

By subtracting Eq. (19) from (7) and neglecting horizontal DSE advection, we can obtain

$$D - \left\langle \omega \frac{\partial h}{\partial p} \right\rangle \simeq \left(\widetilde{\gamma} - \widetilde{\Gamma}_{\mathrm{v}} \right) \left\langle \omega \frac{\partial s}{\partial p} \right\rangle \,. \tag{20}$$

Using these approximations, we can further express Eq. (8) as

$$\frac{\partial \ln P}{\partial t} \propto - \langle \mathbf{v} \cdot \nabla Lq \rangle + \left(\widetilde{\gamma} - \widetilde{\Gamma}_{\mathrm{v}} \right) \left\langle \omega \frac{\partial s}{\partial p} \right\rangle \,. \tag{21}$$

$D - \langle \omega \partial h / \partial p \rangle$ in Eq. (20) is equivalent to the vertically integrated "column process" proposed by Chikira (2014) under the WTG approximation, as discussed further in Section 4b. Thus, Eq. (20) approximates the column process as a linear function of convective intensity. Equation (21) now indicates that the amplification or decay of precipitation is controlled by the balance between horizontal moisture advection and the column process.

Equation (21) can be tested by plotting the probabilities of precipitation amplification as a function of $\langle \mathbf{v} \cdot \nabla Lq \rangle$ and $\langle \omega \partial s / \partial p \rangle$, similarly to Fig. 3. Figure 7 is constructed in the same way as Fig. 3, but the x- and y-axes are replaced with the corresponding quantities in Eq. (21). The bins below the critical line whose slope is $\widetilde{\gamma} - \widetilde{\Gamma}_{\mathrm{v}}$—corresponding to a positive RHS of Eq. (21)—have high probabilities of precipitation amplification (red colors). By contrast, the bins above the $\widetilde{\gamma} - \widetilde{\Gamma}_{\mathrm{v}}$-line—a negative RHS of Eq. (21)—have low probabilities of precipitation amplification (blue colors), meaning that the precipitation will most likely decay in the next day. Thus, the modification of Eq. (8) into Eq. (21) preserves skill in predicting precipitation amplification statistically, especially for the greatest departures from the critical line. We replicated this figure for DJF but found no notable differences from JJA (not shown), except for the values of $\widetilde{\gamma} - \widetilde{\Gamma}_{\mathrm{v}}$, which are shown in Section 3e.

Figure 8 shows the joint distribution of $\langle \mathbf{v} \cdot \nabla Lq \rangle$ and $\langle \omega \partial s / \partial p \rangle$ over each oceanic basin, using the same bins as in Fig. 7. Similarly to Fig. 4, the ridge of the joint PDF approximately follows the critical line (or $\widetilde{\gamma} - \widetilde{\Gamma}_{\mathrm{v}}$-line). In other words, the distribution is concentrated around a condition of $\langle \mathbf{v} \cdot \nabla Lq \rangle = (\widetilde{\gamma} - \widetilde{\Gamma}_{\mathrm{v}}) \langle \omega \partial s / \partial p \rangle$ which is approximately equal to a condition of $\partial \langle q \rangle / \partial t \simeq 0$. This indicates that horizontal moisture advection is commonly balanced by the column process, where convection is in a quasi-steady state. The gray areas in Fig. 7 account for 40%, 46%, 40%, and 50% of the total data points in panels (a)–(d), respectively, consistent with populations commonly near the quasi-steady state. When an atmospheric column is close to this balanced condition,

Fig. 7 doesn't show skill in predicting precipitation amplification or decay. By contrast, when an atmospheric column is far from the balanced condition, values of $\langle \mathbf{v} \cdot \nabla Lq \rangle$ and $\langle \omega \partial s / \partial p \rangle$ predict whether the precipitation will amplify or decay in the next day.

If we alternatively assume that horizontal MSE (or moisture) advection is a linear feedback process whose feedback efficiency is temporally invariant horizontal GMS $\widetilde{\Gamma}_{\mathrm{h}}$, a similar derivation as for Eq. (21) yields

$$\frac{\partial \ln P}{\partial t} \propto -\left\langle \omega \frac{\partial h}{\partial p} \right\rangle + \left(\widetilde{\gamma} - \widetilde{\Gamma}_{\mathrm{h}} \right) \left\langle \omega \frac{\partial s}{\partial p} \right\rangle \quad \text{(invalid)}. \tag{22}$$

This equation is shown to be invalid in Fig. 9, which is constructed in the same way as Fig. 7 except that the y-axis is replaced with $\langle \omega \partial h / \partial p \rangle$ and the slope of the dashed line corresponds to $\widetilde{\gamma} - \widetilde{\Gamma}_{\mathrm{h}}$.

Figure 9 shows that Eq. (22) does not have strong predictive skill compared to Eq. (21) (Fig. 7). Although there is some predictability—sub-critical (super-critical) grid points are slightly red (blue)—the probabilities are much lower than those in Fig. 7. Especially over the Indian Ocean, large imports of MSE due to vertical advection ($\langle \omega \partial h / \partial p \rangle << 0$) do not guarantee an amplification of precipitation—the probability of amplification is close to 50%. This result indicates that the pair of vertical MSE advection and convective intensity are not statistically predictive of the amplification or decay of precipitation in the following day, unlike the pair of horizontal moisture advection and convective intensity.

Equation (21) and Fig. 7 provide us with a simplified view of day-to-day precipitation variability in general. At each location, the column process [the second term on the RHS of Eq. (21)] determines a critical threshold that delineates amplifying and decaying phases of large-scale convective ensembles. When drying due to horizontal moisture advection is less than the threshold, precipitation tends to amplify. Conversely, when this drying is greater than the column-process threshold, precipitation tends to decay. In a quasi-steady state, the environment is in a balanced

condition of $\langle \mathbf{v} \cdot \nabla Lq \rangle = (\widetilde{\gamma} - \widetilde{\Gamma}_{\mathrm{v}}) \langle \omega \partial s / \partial p \rangle$ in which the convective intensity becomes steady. When horizontal moisture advection perturbs this balanced condition, precipitation from a large-scale convective ensemble tends to amplify or decay, depending on the balance between $\langle \mathbf{v} \cdot \nabla Lq \rangle$ and $(\widetilde{\gamma} - \widetilde{\Gamma}_{\mathrm{v}}) \langle \omega \partial s / \partial p \rangle$. This view indicates that the variability of horizontal moisture advection is a primary driver of ubiquitous convective variability in general, and thus, skillful weather prediction in the deep tropics requires skillful prediction of horizontal moisture advection, at least statistically.

In this study, we ignored temporal variations in ω-profile shapes by assuming the vertical GMS to be temporally invariant. In general, ω profiles tend to evolve from a bottom-heavy to top-heavy shape when following a convective lifecycle. However, when an ω profile is bottom heavy in an early stage of a convective system, the amplitude of convection tends to be small. Thus, even though a bottom-heavy circulation imports MSE, its contribution is small, and is overwhelmed by large variability of horizontal MSE (moisture) advection (Fig. 6).

However, this doesn't mean that the variations in ω profiles are unimportant. The variations in ω profiles are of established importance in a Lagrangian framework that follows an individual convective system (as in Fuchs-Stone et al. 2020) or moisture envelope (as in Hannah et al. 2016). In that framework, the contribution of horizontal moisture advection is negligible, and the variations in ω-profile shapes are closely linked to the evolution of a convective system. Therefore, if we were to hypothetically trace an individual convective system and compute a Lagrangian tendency of precipitation, Eq. (22) would explain its amplification and decay well. In an Eulerian framework, by contrast, the contribution of ω-profile shapes may be overwhelmed by a greater variability of horizontal moisture advection. This may be why Fig. 7 contrasts with Inoue and Back (2015b), especially their Fig. 5, where it was suggested that temporal variations in ω-profile shapes are crucial for convective variability. Whereas their lifecycle composite method stressed a

Lagrangian interpretation over many days, here we find that such an interpretation underestimates the contribution of day-to-day horizontal MSE advection in the Eulerian framework.

The negative of $\widetilde{\gamma} - \widetilde{\Gamma}_{\mathrm{v}}$, or $\widetilde{\Gamma}_{\mathrm{v}} - \widetilde{\gamma}$, is often called the "effective GMS" (e.g., Su and Neelin 2002; Bretherton and Sobel 2002; Hannah and Maloney 2014). The effective GMS is a measure of the GMS that includes the effect of the diabatic source term[5]. A positive $\widetilde{\gamma}$ contributes to a positive feedback whereas a positive $\widetilde{\Gamma}_{\mathrm{v}}$, which is a stability index, contributes to damping. Thus, a net positive feedback is represented as $\widetilde{\gamma} - \widetilde{\Gamma}_{\mathrm{v}}$, which is the negative of effective GMS.

The slopes of the regression lines through the origin in Fig. 7 correspond to the effective feedback values, $\widetilde{\gamma} - \widetilde{\Gamma}_{\mathrm{v}}$, which are positive over all of the oceanic basins. This suggests that precipitation tends to increase spontaneously in the absence of horizontal moisture advection [i.e., $\langle \mathbf{v} \cdot \nabla Lq \rangle = 0$ in Eq. (21)]. Past observational studies have found that horizontal import of moist air enhances the initiation and growth of convection whereas import of dry air suppresses convection (see review by Sherwood et al. 2010). Our results go further and indicate that an absence of horizontal moisture advection is sufficient to destabilize the tropical atmosphere, and that the degree of such destabilization can be measured by $\widetilde{\gamma} - \widetilde{\Gamma}_{\mathrm{v}}$.

e. Geographic variability of feedbacks and $\widetilde{\tau}$

The geographic variability of $\widetilde{\gamma}$ (sum of cloud-radiation and convection-surface-flux feedbacks) for JJA has already been discussed in Section 3b. Here we investigate the geographic variability of the remaining feedback parameters in Eq. (21): $\widetilde{\Gamma}_{\mathrm{v}}$ (the vertical GMS; with positive values implying a damping effect due to vertical MSE advection) and $\widetilde{\gamma} - \widetilde{\Gamma}_{\mathrm{v}}$ (a bulk positive feedback; equivalent

[5]In many studies, only the effect of radiative heating is included in the definition of the effective GMS. In this study, we also include the effect of surface evaporation, as in Hannah and Maloney (2014).

to the negative of the effective GMS). We also show the result for DJF. All quantities have been calculated with regression through the origin in each grid cell, following Inoue and Back (2017).

Figure 10(b) shows the geographic pattern of $\widetilde{\Gamma}_{\mathrm{v}}$ for JJA. Since a positive value of $\widetilde{\Gamma}_{\mathrm{v}}$ is associated with damping, the color scale is reversed so that blue colors correspond to a negative feedback. In the Indian Ocean, western Pacific, Mesoamerican region, Africa, and Southeast Asia, $\widetilde{\Gamma}_{\mathrm{v}}$ is positive, which means that the vertical MSE advection in these regions during JJA acts to damp or stabilize convection. By contrast, the central Pacific, Atlantic Ocean, Amazon, the southwestern edge of the Indian Ocean, and the eastern edge of the SPCZ exhibit negative values, which means that the vertical MSE advection in these regions in the boreal summer tends to destabilize convection.

It is expected that the values of $\widetilde{\Gamma}_{\mathrm{v}}$ will be primarily determined by the shape of ω profiles (e.g, Sobel 2007; Raymond et al. 2009; Inoue and Back 2015a,b). In general, a bottom-heavy ω profile is associated with a low or negative value of $\widetilde{\Gamma}_{\mathrm{v}}$ while a top-heavy ω profile is associated with a high value of $\widetilde{\Gamma}_{\mathrm{v}}$. Thus, we compare the values of $\widetilde{\Gamma}_{\mathrm{v}}$ with the top-heaviness ratio $\widetilde{\tau}$ computed as described in Section 2d.

Figure 10(d) shows the geographic pattern of $\widetilde{\tau}$, which can be compared with Fig. 2(b) for the corresponding ω-profile shapes. Consistent with previous studies (e.g., Back and Bretherton 2006, 2009; Back et al. 2017; Inoue et al. 2020), the warm pool region including the Indian Ocean and western Pacific exhibits top-heavy ω profiles (blue colors) whereas the central Pacific and Atlantic Ocean show bottom-heavy profiles (red colors). Additionally, the Mesoamerica region (especially around the Caribbean Sea) shows top-heavy profiles whereas the eastern edge of the SPCZ and the southwestern edge of the Indian Ocean exhibit relatively bottom-heavy profiles during JJA. These geographic patterns of $\widetilde{\tau}$ over oceans derived from ERA-I are largely consistent with cloud-top height and upper-tropospheric hydrometeor coverage observed from satellites (e.g., Mace et al.

2007; Kokhanovsky et al. 2007). Additionally, Africa exhibits high $\widetilde{\tau}$, and South America away from orography exhibits a mixture of slightly positive and negative $\widetilde{\tau}$.

As expected, the top-heavy regions generally have high values of $\widetilde{\Gamma}_{\mathrm{v}}$ whereas the bottom-heavy regions have negative values. A high spatial correlation between $\widetilde{\tau}$ and $\widetilde{\Gamma}_{\mathrm{v}}$ (0.61 over the entire domain and 0.76 over oceans) indicates that the values of $\widetilde{\Gamma}_{\mathrm{v}}$ are in good part explained by the ω-profile shapes. The correlation is reduced by the fact that $\widetilde{\Gamma}_{\mathrm{v}}$ is not a linear function of $\widetilde{\tau}$ (Appendix B). Furthermore, there are other sources of variations in $\widetilde{\Gamma}_{\mathrm{v}}$, such as variations in temperature and moisture profiles (e.g., Yu et al. 1998), as well as geographic variability of ω profiles that is not captured by linear combinations of EOF1 and EOF2.

Figure 10(c) depicts the effective feedback, $\widetilde{\gamma} - \widetilde{\Gamma}_{\mathrm{v}}$. This figure shows that $\widetilde{\gamma} - \widetilde{\Gamma}_{\mathrm{v}}$ is positive almost everywhere in the tropical convergence zones—thus the effective GMS is negative everywhere. This suggests that, in the absence of horizontal moisture advection—as in simulations of radiative convective equilibrium (e.g., Wing et al. 2017)—convective systems may tend to amplify spontaneously through a positive feedback loop everywhere in the tropical convergence zones. A positive $\widetilde{\gamma} - \widetilde{\Gamma}_{\mathrm{v}}$ (or negative effective GMS) is believed to be a necessary condition for the growth of the MJO (e.g., Sobel and Gildor 2003; Fuchs and Raymond 2007; Raymond and Fuchs 2007; Sobel and Maloney 2013; Sugiyama 2009; Adames and Kim 2016), and this condition has been investigated mainly in MJO-oriented studies over the warm pool region. But Fig. 10(c) suggests that this positive feedback happens everywhere in the tropical convergence zones including the central Pacific and Atlantic Ocean where there are no convective signals of the MJO.

During JJA, the Indian Ocean exhibits the strongest positive feedback (the greatest $\widetilde{\gamma} - \widetilde{\Gamma}_{\mathrm{v}}$) due to the greatest $\widetilde{\gamma}$ [Fig. 10(a)], which suggests that it may be relevant to the initiation of the MJO. However, $\widetilde{\gamma} - \widetilde{\Gamma}_{\mathrm{v}}$ shows no peak over the Indian Ocean during DJF when the MJO is most active, instead exhibiting a remarkably homogeneous pattern especially between 15°N–15°S [Fig. 11(c)].

During this season, $\widetilde{\gamma}$ is large over the eastern part of the Indian Ocean and the maritime continental region [Fig. 11(a)], but this is cancelled out by $\widetilde{\Gamma}_{\rm v}$ [Fig. 11(b)], leading to a homogeneous pattern of $\widetilde{\gamma} - \widetilde{\Gamma}_{\rm v}$. Therefore, we conclude that the geographic pattern of $\widetilde{\gamma} - \widetilde{\Gamma}_{\rm v}$ is not associated with MJO initiation over the Indian Ocean, at least in the ERA-I data. This result, however, leaves us with some open questions. Why is $\widetilde{\gamma} - \widetilde{\Gamma}_{\rm v}$ remarkably high over the Indian Ocean only during JJA? How is that pattern related to boreal summer monsoons? Are the values of these feedback parameters consistent across different data sources? These questions will be investigated in future work.

Even though $\widetilde{\tau}$ varies significantly across the different regions [Figs. 10–11(d)], causing $\widetilde{\Gamma}_{\rm v}$ to vary as well [Figs. 10–11(b)], $\widetilde{\gamma} - \widetilde{\Gamma}_{\rm v}$ is remarkably homogeneous except over the JJA Indian Ocean and SPCZ [Figs. 10–11(c)]. In particular, there is no contrast in $\widetilde{\gamma} - \widetilde{\Gamma}_{\rm v}$ between the western Pacific, central Pacific, and Atlantic Ocean, unlike patterns of $\widetilde{\tau}$ and $\widetilde{\Gamma}_{\rm v}$. This is because $\widetilde{\gamma}$ and $\widetilde{\Gamma}_{\rm v}$ are in a see-saw balance.

Figures 10–11(a) and (b) reveal that $\widetilde{\gamma}$ and $\widetilde{\Gamma}_{\rm v}$ are significantly correlated with a spatial correlation of 0.6 for both JJA and DJF. This means that when the positive feedback from the diabatic sources (radiation plus surface fluxes) is strong, the negative feedback due to vertical MSE advection is also strong. Conversely, when the diabatic feedback is weak, the damping effect due to vertical MSE advection is also weak. This see-saw balance leads to a relatively small and homogeneous effective feedback. This balance may be explained, in part, by the relationship between the cloud-radiation feedback and the top-heaviness of ω profiles, which is discussed in Section 4a.

Although $\widetilde{\gamma} - \widetilde{\Gamma}_{\rm v}$ is positive everywhere in the tropical convergence zones, how this net positive feedback is achieved varies across different locations. In the top-heavy regions, the net positive feedback is primarily due to $\widetilde{\gamma}$, the sum of cloud-radiation and convection-surface-flux feedbacks. The net positive feedback there is achieved because the positive effect of $\widetilde{\gamma}$ exceeds the negative effect due to $\widetilde{\Gamma}_{\rm v}$. By contrast, in the bottom-heavy regions, the net positive feedback is achieved

primarily because of the negative $\widetilde{\Gamma}_{\rm v}$ via a lower-tropospheric shallow circulation which imports MSE into an atmospheric column. In these regions, the contribution of $\widetilde{\gamma}$ is small.

4. Discussion

a. Cloud-radiation feedback and omega profiles

In the above investigation, we found that $\widetilde{\gamma}$ and $\widetilde{\Gamma}_{\rm v}$ are in a see-saw balance. Such a balance could be explained partially by the relationship between a cloud-radiation feedback and ω-profile shapes, as claimed by Inoue et al. (2020). As an ω profile becomes top-heavy, the vertical GMS increases. Yet a top-heavy profile, which is generally associated with high coverage of stratiform clouds (e.g., Schumacher and Houze 2003), has a strong cloud-radiation feedback due to a strong greenhouse effect of high clouds. By contrast, when an ω profile is bottom-heavy, the vertical GMS is small, but the cloud greenhouse effect is also small because of lower cloud top heights. Therefore, there may exist a positive correlation between a cloud-radiation feedback and the vertical GMS.

However, this explanation is not complete because it does not include the convection-surface-flux feedback. Moreover, Fig. 10(d) shows that the western Pacific has more top-heavy ω profiles than the Indian Ocean during JJA, but the $\widetilde{\gamma}$ is greater over the Indian Ocean than the western Pacific. Thus, the relationship between a cloud-radiation feedback and the top-heaviness of ω-profiles doesn't explain the contrast of $\widetilde{\gamma}$ between the Indian Ocean and western Pacific during JJA, at least in the merged data examined here. How are ω profiles, a cloud-radiation feedback, and a convection-surface-flux feedback linked? Why and how could $\widetilde{\gamma} - \widetilde{\Gamma}_{\rm v}$ exhibit the greatest value over the Indian Ocean during JJA, but not during DJF? These questions are worthwhile investigating in future work.

b. Perspective of the moisture budget equation

When precipitation happens, is the atmospheric column moistened or dried? Answering this question may not be trivial because although precipitation reaching the surface dries the column, ascending motions associated with convection conversely tend to moisten the atmosphere, counteracting the drying processes.

To address this question in the context of an MJO study, Chikira (2014) introduced the concept of the "column process." If the column-integrated moisture budget equation is rearranged as

$$\frac{\partial \langle Lq \rangle}{\partial t} + \langle \mathbf{v} \cdot \nabla Lq \rangle = \langle C \rangle \ , \tag{23}$$

where

$$\langle C \rangle \equiv -\left\langle \omega \frac{\partial Lq}{\partial p} \right\rangle + LE - LP \, , \tag{24}$$

the column process C combines all the moistening and drying processes happening internally within an atmospheric column. Chikira (2014) found that $\langle C \rangle$ is positively correlated with precipitation in both ERA-I and a global model. This suggests that, in the absence of horizontal moisture advection, the atmosphere tends to be moistened by convection when the effects of precipitation and large-scale ascending motions are combined as the column process. Here the contribution of surface evaporation can be neglected since such moistening is found throughout most of the free troposphere. This column-process feedback was examined in greater detail by subsequent studies (e.g., Wolding and Maloney 2015; Hannah et al. 2016; Janiga and Zhang 2016; Wolding et al. 2016; Adames 2017; Ahmed and Schumacher 2018).

What we have presented here can be equated to this column-process view. Assuming the WTG approximation, and substituting Eq. (20) into the column MSE budget equation yields

$$\frac{\partial \langle Lq \rangle}{\partial t} + \langle \mathbf{v} \cdot \nabla Lq \rangle \simeq \left(\widetilde{\gamma} - \widetilde{\Gamma}_{\mathrm{v}} \right) \left\langle \omega \frac{\partial s}{\partial p} \right\rangle \, . \tag{25}$$

Thus, we obtain

$$\langle C \rangle \simeq D - \left\langle \omega \frac{\partial h}{\partial p} \right\rangle \simeq \left(\widetilde{\gamma} - \widetilde{\Gamma}_{\rm v} \right) \left\langle \omega \frac{\partial s}{\partial p} \right\rangle . \tag{26}$$

Since $\widetilde{\gamma} - \widetilde{\Gamma}_{\rm v}$ is found to be positive nearly universally over the tropical convergence zones examined, these equivalencies suggest that when an ascending motion happens (i.e., $\langle \omega \partial s / \partial p \rangle > 0$), the column process tends to moisten the atmosphere. This is consistent with the findings of Chikira (2014) and the other studies listed above.

However, there are a few novelties in our results. First, while the previous studies have investigated the column-process feedback only in the context of the MJO over the warm pool region, Figs. 10–11(c) suggest that the same positive feedback may occur over the entire tropical convergence zones, not limited to the warm pool region. Second, because we did not apply any temporal filtering to the daily data, the results in this paper suggest that the column-process feedback occurs not only in the MJO, but also in more general convective variability in the tropics. Finally, the expression of the column process as Eq. (26), instead of Eq. (24), reveals that a positive column-process feedback may be achieved in different ways over different locations. In the regions where ω profiles are top-heavy, this is achieved due to strong $\widetilde{\gamma}$. By contrast, in the regions where ω profiles are bottom-heavy, a shallow circulation (or negative $\widetilde{\Gamma}_{\rm v}$) causes the positive feedback.

c. Moisture modes and ubiquitous convective variability

Theoretical literature suggests that the MJO belongs to a "moisture mode" (e.g., Sobel et al. 2001; Sobel and Gildor 2003; Raymond and Fuchs 2007; Sugiyama 2009; Sobel and Maloney 2013; Adames and Kim 2016). A moisture mode appears under the condition of two approximations: (i) the WTG approximation, and (ii) the approximation of precipitation as a function of column water vapor. Yet these approximations are identical to the ones employed in this study. In fact, a linearized version of Eq. (21) is the core of the moisture mode theories. Therefore, we conclude

that the convective amplification mechanism discussed in this study is identical to the core of the moisture-mode instability.

However, the variability investigated in this study is not limited to the MJO for the following reasons. First, Fig. 7 shows that the framework of Eq. (21) applies even in the central Pacific and Atlantic Ocean where there are no MJO convective signals. Second, we replicated Fig. 7 for a time period when the MJO is suppressed, and found that it still exhibits predictive skill for convective amplification and decay (not shown). Third, the result in Fig. 7 includes all convective variability whose timescale is longer than two days (the Nyquist frequency of daily data). Because the metric in this figure (probability) is independent of the amplitude of the signals, it won't be contaminated by longer-timescale variability. Thus, we can claim that Eq. (21) applies generally to convective variability whose timescale is longer than two days.

Based on those results, we claim that most of ubiquitous convective variability over the maritime tropical convergence zones (including mesoscale convective systems), which may collectively be called random noise, may amplify with the same mechanism as the moisture-mode instability. This idea has been also suggested by Fuchs and Raymond (2017). One of the exceptions may be convectively coupled gravity waves including the Kelvin, inertio-gravity, and mixed Rossby-gravity waves (e.g., Matsuno 1966). Existing literature suggests that convectively coupled gravity waves are governed by a different mechanism than that of the moisture mode. For instance, temporal variations in temperature, which are ignored in this study, play a crucial role in the instability (e.g., Mapes 2000; Khouider and Majda 2006; Raymond and Fuchs 2007; Kuang 2008; Herman et al. 2016; Wolding et al. 2020). In addition, the MSE and moisture budgets behave differently in these gravity waves (e.g., Yasunaga and Mapes 2012a,b; Inoue and Back 2015a; Ahmed and Schumacher 2018). However, the high predictability in Fig. 7 may indicate that most tropical convective variability behaves like a moisture mode.

d. Caveats

Our results depend on a few caveats. The main one is the fidelity of ERA-I and in particular of ERA-I's ω profiles. These are simulated by the Cy31r1 ECMWF Integrated Forecasting System, which suffers from biases in convective variability (Bechtold et al. 2008). Additionally, due to the discrepancy between data assimilation and model simulations, ERA-I's energy and moisture budgets have substantial residuals that are coherent with convective activity (e.g., Kim et al. 2014; Yasunaga et al. 2019). These coherent residuals can affect the values of $\widetilde{\gamma}$, $\widetilde{\Gamma}_{\mathrm{v}}$, and $\widetilde{\gamma} - \widetilde{\Gamma}_{\mathrm{v}}$. We will reevaluate these parameters with independent data sets in future work.

A second caveat derives from the omission of known features of natural convection, such as the enhanced sensitivity of moist convection to lower-tropospheric moisture perturbations compared to upper-tropospheric ones (e.g., Holloway and Neelin 2009; Kuang 2010; Tulich and Mapes 2010; Wang and Sobel 2012). This fact was omitted when we developed a theory based on column-integrated quantities. We also neglected temperature perturbations, which affect convective intensity by modulating entrainment buoyancy (e.g., Ahmed and Neelin 2018). In spite of these simplifications, our parsimonious theory remains statistically predictive of day-to-day precipitation variability, indicating that it still captures a core aspect of tropical convective variability.

5. Summary and conclusions

This study used 1998-2012 ERA-I reanalysis and TRMM3B42 precipitation data to extend the diagnostic framework proposed by IB17 and address the following questions:

1. What roles do horizontal and vertical MSE advection play in controlling day-to-day convective variability?

2. How do those roles differ geographically?

Our analysis focused on the tropical convergence zones during June-July-August (JJA) and December-January-February (DJF).

We diagnosed the distributions of total, horizontal, and vertical MSE advection, and found that over all the oceanic basins including the Indian, western Pacific, central Pacific, and Atlantic Oceans, the variability of total MSE advection is predominantly explained by the variability of horizontal MSE advection.

We derived a simple expression for precipitation variability [Eq. (21)] with two assumptions. (1) Vertical MSE advection behaves as a simple linear feedback, whose feedback coefficient is the vertical GMS, $\widetilde{\Gamma}_{\mathrm{v}}$, which varies geographically and seasonally. This implicitly assumes that local temporal variations in ω-profile shapes are negligible on subseasonal timescales. (2) The diabatic source term (radiation plus surface fluxes) amplifies linearly as a function of convective intensity. The rate of the amplification, $\widetilde{\gamma}$, is the sum of a cloud-radiation feedback and a convection-surface-flux feedback, which also varies geographically and seasonally, but not day to day.

In a quasi-steady state, the atmosphere can be considered in a balanced condition of $\langle \mathbf{v} \cdot \nabla Lq \rangle = (\widetilde{\gamma} - \widetilde{\Gamma}_{\mathrm{v}}) \langle \omega \partial s / \partial p \rangle$. In this condition, horizontal moisture advection is balanced by the spontaneous accumulation of moisture due to positive feedbacks. The variability of large-scale ensemble precipitation is then dependent on departures of the environment from this balanced condition. $(\widetilde{\gamma} - \widetilde{\Gamma}_{\mathrm{v}}) \langle \omega \partial s / \partial p \rangle$ is equivalent to a vertically integrated "column process" (Chikira 2014). When drying due to horizontal moisture advection is less or greater than the spontaneous growth due to the column process, large-scale averaged precipitation tends to amplify or decay, respectively. This view indicates that the variability of horizontal moisture advection is a primary driver of ubiquitous convective variability in general, and that skillful prediction of horizontal moisture advection is required for skillful weather prediction in the deep tropics.

We also investigated the geographic variability of the effective GMS. We found that the effective GMS is negative over almost all tropical convergence regions. This indicates that in the absence of horizontal moisture advection, convection tends to amplify spontaneously through a positive column-process feedback. Generally, such a positive feedback has been considered as a necessary condition for the growth of the MJO. But our study indicates that this may occur throughout the tropics, not limited to the warm pool region, and in ubiquitous convective variability, not limited to the MJO. Even though the effective GMS is nearly universally negative, how that is achieved varies geographically, depending on the shape of climatological ω profiles. In regions where ω profiles are top-heavy, the negative effective GMS is preferentially achieved due to strong feedbacks between convection and the diabatic source term. In these regions, the vertical MSE advection stabilizes convective systems—the vertical GMS is positive. By contrast, in bottom-heavy regions, the negative effective GMS is due to the negative vertical GMS, which represents the import of MSE through a bottom-heavy circulation. In these regions, the contribution of diabatic feedbacks is small.

Except for the JJA Indian Ocean and SPCZ, the effective GMS is largely homogeneous spatially. In particular, it is remarkably homogeneous during DJF. This is because the diabatic feedback and the vertical GMS are in a see-saw balance. When the diabatic feedback term is large, the vertical GMS, which is a negative feedback, is also large, canceling out the positive effect. Conversely, when the diabatic feedback is small, the vertical GMS is also small. Thus, these balances lead to a relatively small and homogeneous effective GMS.

The convective amplification mechanism discussed in this study has many similarities with the moisture-mode instability. In fact, the key equation in this study [Eq. (21)] is at the core of the moisture-mode theories. Based on these results, we therefore speculate that the moisture-mode

instability mechanism is also responsible for amplification of more general convective variability, not limited to the MJO.

This study indicates that ubiquitous convective variability can be sufficiently explained with a MSE-based or thermodynamical framework, supporting previous theoretical attempts (e.g,. Neelin and Zeng 2000; Sobel and Bretherton 2000). What type of convective variability is NOT explained by the MSE-based framework? One likely example is the convectively coupled gravity waves. Another might be tropical continental convection with strong diurnal cycles. This question will be addressed in future studies.

Acknowledgments. The authors thank Larissa Back, Adam Sobel, and Hiro Masunaga for useful discussions. Many insightful comments and suggestions by Fiaz Ahmed and two anonymous reviewers improved our manuscript significantly. KI was supported by an appointment to the NASA Postdoctoral Program at the NASA Goddard Institute for Space Studies, administered by Universities Space Research Association. MB was supported in part by NSF (AGS-1565522). AF was supported by the NASA Modeling, Analysis and Prediction Program.

Data availability statement. We obtained ERA-I data sets from the Research Data Archive (`https://rda.ucar.edu`) and TRMM 3B42 precipitation data from `https://gpm.nasa.gov/data-access/downloads/trmm`.

APPENDIX A

Precipitation-CWV relationship

Here we examine the assumption of Eq. (6). Figure A1 shows the relationship between $\partial \ln P/\partial t$ and $\partial \langle q \rangle / \partial t$. The tendencies are computed using a centered difference. For instance, the log

precipitation tendency at time j was computed as

$$\frac{1}{2\Delta t}\ln\left(\frac{P_{j+1}}{P_{j-1}}\right) \tag{A1}$$

where Δt is one day. We excluded the singularity of $P_{j-1} = 0$.

In Fig. A1, there is a robust positive correlation between the log precipitation tendency and the CWV tendency computed over two days. This relationship holds across all of the oceanic basins. This indicates that the exponential relationship between precipitation and CWV proposed by Bretherton et al. (2004) is statistically valid not only in a longer-term climatology, but also for day-to-day convective variability. Thus, the CWV variability is a good predictor of precipitation variability, which can serve to simplify the conceptual understanding of convective variability.

APPENDIX B

Relation between $\widetilde{\Gamma}_{\mathrm{v}}$ and $\widetilde{\tau}$

If we assume that DSE and MSE profiles are fixed over the tropical convergence zones (denoted as s_0 and h_0) values of $\widetilde{\Gamma}_{\mathrm{v}}$ are solely determined by ω-profile shapes. When we approximate ω as Eq. (12), Eq. (19) can be written as

$$o_1 G_{1,h} + o_2 G_{2,h} = \widetilde{\Gamma}_{\mathrm{v}}\left(o_1 G_{1,s} + o_2 G_{2,s}\right) , \tag{B1}$$

where $G_{j,h} \equiv \left\langle \Omega_j \partial h_0/\partial p \right\rangle$ and $G_{j,s} \equiv \left\langle \Omega_j \partial s_0/\partial p \right\rangle$ for $j = 1,2$. This relation is also held for anomalies, but we omit prime marks for brevity. Multiplying the both sides by $o_1 G_{1,s} + o_2 G_{2,s}$, taking a time average, and solving for $\widetilde{\Gamma}_{\mathrm{v}}$ yields

$$\widetilde{\Gamma}_{\mathrm{v}} = \frac{G_{1,h}G_{1,s} + \widetilde{\tau}\left(G_{1,h}G_{2,s} + G_{2,h}G_{1,s}\right) + \widetilde{\tau}^2 G_{2,h}G_{2,s}}{G_{1,s}^2 + 2\widetilde{\tau}G_{1_s}G_{2,s} + \widetilde{\tau}^2 G_{2,s}^2} . \tag{B2}$$

Here we used the definition of $\widetilde{\tau}$ in Eqs. (13)–(14). Equation (B2) shows that $\widetilde{\Gamma}_{\mathrm{v}}$ is a nonlinear function of $\widetilde{\tau}$.

References

Adames, Á. F., 2017: Precipitation Budget of the Madden–Julian Oscillation. *J. Atmos. Sci.*, **74 (6)**, 1799–1817, doi:10.1175/JAS-D-16-0242.1.

Adames, Á. F., and D. Kim, 2016: The MJO as a Dispersive, Convectively Coupled Moisture Wave: Theory and Observations. *J. Atmos. Sci.*, **73**, 913–941, doi:10.1175/JAS-D-15-0170.1.

Ahmed, F., and J. D. Neelin, 2018: Reverse Engineering the Tropical Precipitation–Buoyancy Relationship. *J. Atmos. Sci.*, **75 (5)**, 1587–1608, doi:10.1175/JAS-D-17-0333.1.

Ahmed, F., and C. Schumacher, 2018: Spectral Signatures of Moisture–Convection Feedbacks over the Indian Ocean. *J. Atmos. Sci.*, **75**, 1995–2015, doi:10.1175/JAS-D-17-0138.1.

Andersen, J. A., and Z. Kuang, 2011: Moist static energy budget of MJO-like disturbances in the atmosphere of a zonally symmetric aquaplanet. *J. Climate*, **25**, 2782–2804, doi:10.1175/JCLI-D-11-00168.1.

Araligidad, N. M., and E. D. Maloney, 2008: Wind-driven latent heat flux and the intraseasonal oscillation. *Geophys. Res. Lett.*, **35**, L04 815, doi:10.1029/2007GL032746.

Arnold, N. P., M. Branson, Z. Kuang, D. A. Randall, and E. Tziperman, 2015: MJO Intensification with Warming in the Superparameterized CESM. *J. Climate*, **28**, 2706–2724, doi:10.1175/JCLI-D-14-00494.1, URL http://journals.ametsoc.org/doi/full/10.1175/JCLI-D-14-00494.1.

Back, L. E., and C. S. Bretherton, 2005: The relationship between wind speed and precipitation in the pacific ITCZ. *J. Climate*, **18**, 4317–4328, doi:10.1175/JCLI3519.1.

Back, L. E., and C. S. Bretherton, 2006: Geographic variability in the export of moist static energy and vertical motion profiles in the tropical Pacific. *Geophys. Res. Lett.*, **33**, L17 810, doi:10.1029/2006GL026672.

730 Back, L. E., and C. S. Bretherton, 2009: A Simple Model of Climatological Rainfall
731 and Vertical Motion Patterns over the Tropical Oceans. *J. Climate*, **22**, 6477–6497, doi:
732 10.1175/2009JCLI2393.1.

733 Back, L. E., Z. Hansen, and Z. Handlos, 2017: Estimating Vertical Motion Profile Top-Heaviness:
734 Reanalysis Compared to Satellite-Based Observations and Stratiform Rain Fraction. *J. Atmos.*
735 *Sci.*, **74**, 855–864, doi:10.1175/JAS-D-16-0062.1.

736 Bechtold, P., M. Köhler, T. Jung, F. Doblas-Reyes, M. Leutbecher, M. J. Rodwell, F. Vitart,
737 and G. Balsamo, 2008: Advances in simulating atmospheric variability with the ECMWF
738 model: From synoptic to decadal time-scales. *Quart. J. Roy. Meteor. Soc.*, **134**, 1337–1351,
739 doi:10.1002/qj.289.

740 Benedict, J. J., B. Medeiros, A. C. Clement, and J. G. Olson, 2020: Investigating the Role of
741 Cloud-Radiation Interactions in Subseasonal Tropical Disturbances. *Geophys. Res. Lett.*, **47**,
742 e2019GL086 817, doi:10.1029/2019GL086817.

743 Bretherton, C. S., M. E. Peters, and L. E. Back, 2004: Relationships between water vapor path and
744 precipitation over the tropical oceans. *J. Climate*, **17**, 1517–1528, doi:10.1175/1520-0442(2004)
745 017<1517:RBWVPA>2.0.CO;2.

746 Bretherton, C. S., and P. K. Smolarkiewicz, 1989: Gravity waves, compensating subsidence and
747 detrainment around cumulus clouds. *J. Atmos. Sci.*, **46**, 740–759, doi:10.1175/1520-0469(1989)
748 046<0740:GWCSAD>2.0.CO;2.

749 Bretherton, C. S., and A. H. Sobel, 2002: A Simple Model of a Convectively Coupled Walker
750 Circulation Using the Weak Temperature Gradient Approximation. *J. Climate*, **15**, 2907–2920,
751 doi:10.1175/1520-0442(2002)015<2907:ASMOAC>2.0.CO;2.

Chikira, M., 2014: Eastward-Propagating Intraseasonal Oscillation Represented by Chikira-Sugiyama Cumulus Parameterization. Part II: Understanding Moisture Variation under Weak Temperature Gradient Balance. *J. Atmos. Sci.*, **71**, 615–639, doi:10.1175/JAS-D-13-038.1.

Dee, D. P., and Coauthors, 2011: The ERA-Interim reanalysis: configuration and performance of the data assimilation system. *Quart. J. Roy. Meteor. Soc.*, **137**, 553–597, doi:10.1002/qj.828.

Dellaripa, E. M. R., and E. D. Maloney, 2015: Analysis of MJO Wind-Flux Feedbacks in the Indian Ocean Using RAMA Buoy Observations. *J. Meteor. Soc. Japan*, **93A**, 1–20, doi:10.2151/jmsj.2015-021.

Fridlind, A. M., and Coauthors, 2012: A comparison of TWP-ICE observational data with cloud-resolving model results. *J. Geophys. Res. Atmos.*, **117**, D05 204, doi:10.1029/2011JD016595.

Fuchs, Ž., and D. J. Raymond, 2007: A simple, vertically resolved model of tropical disturbances with a humidity closure. *Tellus*, **59**, 344–354, doi:10.1111/j.1600-0870.2007.00230.x.

Fuchs, Ž., and D. J. Raymond, 2017: A simple model of intraseasonal oscillations. *J. Adv. Model. Earth Syst.*, **9**, 1195–1211, doi:10.1002/2017MS000963.

Fuchs-Stone, Ž., D. J. Raymond, and S. Sentić, 2020: OTREC2019: Convection Over the East Pacific and Southwest Caribbean. *Geophys. Res. Lett.*, **47**, e2020GL087 564, doi:10.1029/2020GL087564.

Hannah, W. M., and E. D. Maloney, 2014: The moist static energy budget in NCAR CAM5 hindcasts during DYNAMO. *J. Adv. Model. Earth Syst.*, **6**, 420–440, doi:10.1002/2013MS000272.

Hannah, W. M., B. E. Mapes, and G. S. Elsaesser, 2016: A Lagrangian View of Moisture Dynamics during DYNAMO. *J. Atmos. Sci.*, **73**, 1967–1985, doi:10.1175/JAS-D-15-0243.1.

Herman, M. J., Ž. Fuchs, D. J. Raymond, and P. Bechtold, 2016: Convectively Coupled Kelvin Waves: From Linear Theory to Global Models. *J. Atmos. Sci.*, **73**, 407–428, doi:10.1175/JAS-D-15-0153.1.

Holloway, C. E., and J. D. Neelin, 2009: Moisture Vertical Structure, Column Water Vapor, and Tropical Deep Convection. *J. Atmos. Sci.*, **66**, 1665–1683, doi:10.1175/2008JAS2806.1.

Huffman, G. J., R. F. Adler, D. T. Bolvin, and E. J. Nelkin, 2010: The TRMM Multi-Satellite Precipitation Analysis (TMPA). *Satellite Rainfall Applications for Surface Hydrology*, M. Gebremichael, and F. Hossain, Eds., Springer Netherlands, 3–22.

Huffman, G. J., and Coauthors, 2007: The TRMM Multisatellite Precipitation Analysis (TMPA): Quasi-Global, Multiyear, Combined-Sensor Precipitation Estimates at Fine Scales. *J. Hydrometeor.*, **8**, 38–55, doi:10.1175/JHM560.1.

Inoue, K., Á. F. Adames, and K. Yasunaga, 2020: Vertical Velocity Profiles in Convectively Coupled Equatorial Waves and MJO: New Diagnoses of Vertical Velocity Profiles in the Wavenumber-Frequency Domain. *J. Atmos. Sci.*, doi:10.1175/JAS-D-19-0209.1.

Inoue, K., and L. Back, 2015a: Column-Integrated Moist Static Energy Budget Analysis on Various Time Scales during TOGA COARE. *J. Atmos. Sci.*, **72**, 1856–1871, doi:10.1175/JAS-D-14-0249.1.

Inoue, K., and L. E. Back, 2015b: Gross Moist Stability Assessment during TOGA COARE: Various Interpretations of Gross Moist Stability. *J. Atmos. Sci.*, **72**, 4148–4166, doi:10.1175/JAS-D-15-0092.1.

Inoue, K., and L. E. Back, 2017: Gross Moist Stability Analysis: Assessment of Satellite-Based Products in the GMS Plane. *J. Atmos. Sci.*, **74**, 1819–1837, doi:10.1175/JAS-D-16-0218.1.

795 Janiga, M. A., and C. Zhang, 2016: MJO Moisture Budget during DYNAMO in a Cloud-Resolving
796 Model. *J. Atmos. Sci.*, **73**, 2257–2278, doi:10.1175/JAS-D-14-0379.1.

797 Johnson, R. H., and P. E. Ciesielski, 2000: Rainfall and Radiative Heating Rates from TOGA
798 COARE Atmospheric Budgets. *J. Atmos. Sci.*, **57**, 1497–1514, doi:10.1175/1520-0469(2000)
799 057<1497:RARHRF>2.0.CO;2.

800 Jones, P. W., 1999: First- and Second-Order Conservative Remapping Schemes for Grids in Spher-
801 ical Coordinates. *Mon. Wea. Rev.*, **127**, 2204–2210, doi:10.1175/1520-0493(1999)127<2204:
802 FASOCR>2.0.CO;2.

803 Khouider, B., and A. J. Majda, 2006: A Simple Multicloud Parameterization for Convectively
804 Coupled Tropical Waves. Part I: Linear Analysis. *J. Atmos. Sci.*, **63**, 1308–1323, doi:10.1175/
805 JAS3677.1.

806 Kim, D., J.-S. Kug, and A. H. Sobel, 2014: Propagating versus nonpropagating Madden-Julian
807 oscillation events. *J. Climate*, **27**, 111–125, doi:10.1175/JCLI-D-13-00084.1.

808 Kiranmayi, L., and E. D. Maloney, 2011: Intraseasonal moist static energy budget in reanalysis
809 data. *J. Geophys. Res. Atmos.*, **116**, D21 117, doi:10.1029/2011JD016031.

810 Kokhanovsky, A. A., M. Vountas, V. V. Rozanov, W. Lotz, H. Bovensmann, and J. P. Burrows, 2007:
811 Global cloud top height and thermodynamic phase distributions as obtained by SCIAMACHY
812 on ENVISAT. *International Journal of Remote Sensing*, **28 (20)**, 4499–4507, doi:10.1080/
813 01431160701250366.

814 Kuang, Z., 2008: A moisture-stratiform instability for convectively coupled waves. *J. Atmos. Sci.*,
815 **65**, 834–854, doi:10.1175/2007JAS2444.1.

Kuang, Z., 2010: Linear Response Functions of a Cumulus Ensemble to Temperature and Moisture Perturbations and Implications for the Dynamics of Convectively Coupled Waves. *J. Atmos. Sci.*, **67**, 941–962, doi:10.1175/2009JAS3260.1.

Lin, J.-L., and B. E. Mapes, 2004: Radiation Budget of the Tropical Intraseasonal Oscillation. *J. Atmos. Sci.*, **61**, 2050–2062, doi:10.1175/1520-0469(2004)061<2050:RBOTTI>2.0.CO;2.

Ma, D., A. H. Sobel, Z. Kuang, M. S. Singh, and J. Nie, 2019: A Moist Entropy Budget View of the South Asian Summer Monsoon Onset. *Geophys. Res. Lett.*, **46**, 4476–4484, doi:10.1029/2019GL082089.

Mace, G. G., R. Marchand, Q. Zhang, and G. Stephens, 2007: Global hydrometeor occurrence as observed by CloudSat: Initial observations from summer 2006. *Geophys. Res. Lett.*, **34**, doi:10.1029/2006GL029017.

Madden, R. A., and P. R. Julian, 1971: Detection of a 40–50 Day Oscillation in the Zonal Wind in the Tropical Pacific. *J. Atmos. Sci.*, **28**, 702–708, doi:10.1175/1520-0469(1971)028<0702:DOADOI>2.0.CO;2.

Madden, R. A., and P. R. Julian, 1972: Description of Global-Scale Circulation Cells in the Tropics with a 40–50 Day Period. *J. Atmos. Sci.*, **29**, 1109–1123, doi:10.1175/1520-0469(1972)029<1109:DOGSCC>2.0.CO;2.

Maloney, E. D., 2009: The moist static energy budget of a composite tropical intraseasonal oscillation in a climate model. *J. Climate*, **22**, 711–729, doi:10.1175/2008JCLI2542.1.

Maloney, E. D., and S. K. Esbensen, 2007: Satellite and Buoy Observations of Boreal Summer Intraseasonal Variability in the Tropical Northeast Pacific. *Mon. Wea. Rev.*, **135**, 3–19, doi:10.1175/MWR3271.1.

838 Maloney, E. D., A. H. Sobel, and W. M. Hannah, 2010: Intraseasonal Variability in an Aquaplanet
839 General Circulation Model. *J. Adv. Model. Earth Syst.*, **2**, 5, doi:10.3894/JAMES.2010.2.5.

840 Mapes, B., S. Tulich, J. Lin, and P. Zuidema, 2006: The mesoscale convection life cycle: Building
841 block or prototype for large-scale tropical waves? *Dyn. Atmos. Oceans*, **42**, 3–29, doi:10.1016/
842 j.dynatmoce.2006.03.003.

843 Mapes, B. E., 2000: Convective inhibition, subgrid-scale triggering energy, and stratiform instabil-
844 ity in a toy tropical wave model. *J. Atmos. Sci.*, **57**, 1515–1535, doi:10.1175/1520-0469(2000)
845 057<1515:CISSTE>2.0.CO;2.

846 Mapes, B. E., E. S. Chung, W. M. Hannah, H. Masunaga, A. J. Wimmers, and C. S. Velden,
847 2018: The Meandering Margin of the Meteorological Moist Tropics. *Geophys. Res. Lett.*, **45**,
848 1177–1184, doi:10.1002/2017GL076440.

849 Masunaga, H., and T. S. L'Ecuyer, 2014: A mechanism of tropical convection inferred from
850 observed variability in the moist static energy budget. *J. Atmos. Sci.*, **71**, 3747–3766, doi:
851 10.1175/JAS-D-14-0015.1.

852 Matsuno, T., 1966: Quasi-geostrophic motions in the equatorial area. *J. Meteor. Soc. Japan*, **44**,
853 25–42.

854 Neelin, J. D., and I. M. Held, 1987: Modeling tropical convergence based on the moist static energy
855 budget. *Mon. Wea. Rev.*, **115**, 3–12, doi:10.1175/1520-0493(1987)115<0003:MTCBOT>2.0.
856 CO;2.

857 Neelin, J. D., and N. Zeng, 2000: A quasi-equilibrium tropical circulation model-formulation*. *J.*
858 *Atmos. Sci.*, **57**, 1741–1766, doi:10.1175/1520-0469(2000)057<1741:AQETCM>2.0.CO;2.

Peters, M. E., and C. S. Bretherton, 2005: A Simplified Model of the Walker Circulation with an Interactive Ocean Mixed Layer and Cloud-Radiative Feedbacks. *J. Climate*, **18**, 4216–4234, doi:10.1175/JCLI3534.1.

Raymond, D. J., 1995: Regulation of Moist Convection over the West Pacific Warm Pool. *J. Atmos. Sci.*, **52**, 3945–3959, doi:10.1175/1520-0469(1995)052<3945:ROMCOT>2.0.CO;2.

Raymond, D. J., C. S. Bretherton, and J. Molinari, 2006: Dynamics of the Intertropical Convergence Zone of the East Pacific. *J. Atmos. Sci.*, **63**, 582–597, doi:10.1175/JAS3642.1.

Raymond, D. J., and Ž. Fuchs, 2007: Convectively coupled gravity and moisture modes in a simple atmospheric model. *Tellus*, **59**, 627–640, doi:10.1111/j.1600-0870.2007.00268.x.

Raymond, D. J., G. B. Raga, C. S. Bretherton, J. Molinari, C. López-Carrillo, and Ž. Fuchs, 2003: Convective Forcing in the Intertropical Convergence Zone of the Eastern Pacific. *J. Atmos. Sci.*, **60**, 2064–2082, doi:10.1175/1520-0469(2003)060<2064:CFITIC>2.0.CO;2.

Raymond, D. J., S. L. Sessions, A. H. Sobel, and Ž. Fuchs, 2009: The mechanics of gross moist stability. *J. Adv. Model. Earth Syst.*, **1**, 9, doi:10.3894/JAMES.2009.1.9.

Redelsperger, J.-L., F. Guichard, and S. Mondon, 2000: A Parameterization of Mesoscale Enhancement of Surface Fluxes for Large-Scale Models. *J. Climate*, **13**, 402–421, doi:10.1175/1520-0442(2000)013<0402:APOMEO>2.0.CO;2.

Schumacher, C., and R. A. Houze, 2003: Stratiform Rain in the Tropics as Seen by the TRMM Precipitation Radar. *J. Climate*, **16**, 1739–1756, doi:10.1175/1520-0442(2003)016<1739:SRITTA>2.0.CO;2.

Seager, R., and N. Henderson, 2013: Diagnostic Computation of Moisture Budgets in the ERA-Interim Reanalysis with Reference to Analysis of CMIP-Archived Atmospheric Model Data. *J. Climate*, **26**, 7876–7901, doi:10.1175/JCLI-D-13-00018.1.

Sherwood, S. C., R. Roca, T. M. Weckwerth, and N. G. Andronova, 2010: Tropospheric water vapor, convection, and climate. *Rev. Geophys.*, **48**, doi:10.1029/2009RG000301.

Sobel, A., and E. Maloney, 2013: Moisture modes and the eastward propagation of the MJO. *J. Atmos. Sci.*, **70**, 187–192, doi:10.1175/JAS-D-12-0189.1.

Sobel, A., S. Wang, and D. Kim, 2014: Moist static energy budget of the MJO during DYNAMO. *J. Atmos. Sci.*, **71**, 4276–4291, doi:10.1175/JAS-D-14-0052.1.

Sobel, A. H., 2007: Simple models of ensemble-averaged precipitation and surface wind, given the SST. *The Global Circulation of the Atmosphere*, T. Schneider, and A. H. Sobel, Eds., Princeton University Press, 219–251.

Sobel, A. H., and C. S. Bretherton, 2000: Modeling tropical precipitation in a single column. *J. Climate*, **13**, 4378–4392, doi:10.1175/1520-0442(2000)013<4378:MTPIAS>2.0.CO;2.

Sobel, A. H., and H. Gildor, 2003: A Simple Time-Dependent Model of SST Hot Spots. *J. Climate*, **16**, 3978–3992, doi:10.1175/1520-0442(2003)016<3978:ASTMOS>2.0.CO;2.

Sobel, A. H., J. Nilsson, and L. M. Polvani, 2001: The Weak Temperature Gradient Approximation and Balanced Tropical Moisture Waves*. *J. Atmos. Sci.*, **58**, 3650–3665, doi:10.1175/1520-0469(2001)058<3650:TWTGAA>2.0.CO;2.

Su, H., and J. D. Neelin, 2002: Teleconnection Mechanisms for Tropical Pacific Descent Anomalies during El Nino*. *J. Atmos. Sci.*, **59**, 2694–2712, doi:10.1175/1520-0469(2002)059<2694:TMFTPD>2.0.CO;2.

Sugiyama, M., 2009: The moisture mode in the quasi-equilibrium tropical circulation model. part I: Analysis based on the weak temperature gradient approximation. *J. Atmos. Sci.*, **66**, 1507–1523, doi:10.1175/2008JAS2690.1.

Tulich, S. N., and B. E. Mapes, 2010: Transient Environmental Sensitivities of Explicitly Simulated Tropical Convection. *J. Atmos. Sci.*, **67**, 923–940, doi:10.1175/2009JAS3277.1.

Wang, S., and A. H. Sobel, 2012: Impact of imposed drying on deep convection in a cloud-resolving model. *J. Geophys. Res. Atmos.*, **117**, doi:10.1029/2011JD016847.

Wing, A. A., K. Emanuel, C. E. Holloway, and C. Muller, 2017: Convective Self-Aggregation in Numerical Simulations: A Review. *Surveys in Geophysics*, **38**, 1173–1197, doi:10.1007/s10712-017-9408-4.

Wolding, B., J. Dias, G. Kiladis, E. Maloney, and M. Branson, 2020: Interactions between Moisture and Tropical Convection. Part II: The Convective Coupling of Equatorial Waves. *J. Atmos. Sci.*, **77**, 1801–1819, doi:10.1175/JAS-D-19-0226.1.

Wolding, B. O., and E. D. Maloney, 2015: Objective Diagnostics and the Madden–Julian Oscillation. Part II: Application to Moist Static Energy and Moisture Budgets. *J. Climate*, **28**, 7786–7808, doi:10.1175/JCLI-D-14-00689.1.

Wolding, B. O., E. D. Maloney, and M. Branson, 2016: Vertically resolved weak temperature gradient analysis of the Madden-Julian Oscillation in SP-CESM. *J. Adv. Model. Earth Syst.*, **8**, 1586–1619, doi:10.1002/2016MS000724.

Yasunaga, K., and B. Mapes, 2012a: Differences between More Divergent and More Rotational Types of Convectively Coupled Equatorial Waves. Part I: Space–Time Spectral Analyses. *J. Atmos. Sci.*, **69**, 3–16, doi:10.1175/JAS-D-11-033.1.

Yasunaga, K., and B. Mapes, 2012b: Differences between More Divergent and More Rotational Types of Convectively Coupled Equatorial Waves. Part II: Composite Analysis based on Space-Time Filtering. *J. Atmos. Sci.*, **69**, 17–34, doi:10.1175/JAS-D-11-034.1.

Yasunaga, K., S. Yokoi, K. Inoue, and B. E. Mapes, 2019: Space–Time Spectral Analysis of the Moist Static Energy Budget Equation. *J. Climate*, **32**, 501–529, doi:10.1175/JCLI-D-18-0334.1.

Yokoi, S., and A. H. Sobel, 2015: Intraseasonal Variability and Seasonal March of the Moist Static Energy Budget over the Eastern Maritime Continent during CINDY2011/DYNAMO. *J. Meteor. Soc. Japan*, **93A**, 81–100, doi:10.2151/jmsj.2015-041.

Yu, J., C. Chou, and J. D. Neelin, 1998: Estimating the gross moist stability of the tropical atmosphere*. *J. Atmos. Sci.*, **55**, 1354–1372, doi:10.1175/1520-0469(1998)055<1354:ETGMSO>2.0.CO;2.

Yu, L., and R. A. Weller, 2007: Objectively analyzed air-sea heat fluxes for the global ice-free oceans (1981-2005). *Bull. Amer. Meteor. Soc.*, **88**, 527–539, doi:10.1175/BAMS-88-4-527.

LIST OF TABLES

TABLE 1. Means and variances of MSE advective terms for each basin.

Basin	Advection	Mean [W/m^2]	Variance [(W/m^2)^2*10^4]
IO	$\nabla \cdot \langle h\mathbf{v} \rangle$	91.5	1.81
	$\langle \mathbf{v} \cdot \nabla h \rangle$	58.0	1.52
	$\langle \omega \partial h/\partial p \rangle$	33.5	0.38
WP	$\nabla \cdot \langle h\mathbf{v} \rangle$	80.0	1.96
	$\langle \mathbf{v} \cdot \nabla h \rangle$	38.0	1.40
	$\langle \omega \partial h/\partial p \rangle$	42.0	0.40
CP	$\nabla \cdot \langle h\mathbf{v} \rangle$	7.6	3.20
	$\langle \mathbf{v} \cdot \nabla h \rangle$	45.5	2.80
	$\langle \omega \partial h/\partial p \rangle$	-37.9	0.34
AO	$\nabla \cdot \langle h\mathbf{v} \rangle$	19.3	2.43
	$\langle \mathbf{v} \cdot \nabla h \rangle$	38.4	2.16
	$\langle \omega \partial h/\partial p \rangle$	-19.1	0.27

LIST OF FIGURES

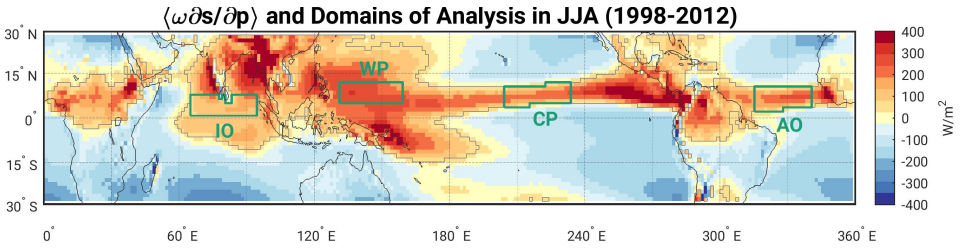

976 FIG. 1. Mean $\langle \omega \partial s/\partial p \rangle$ during June-July-August (JJA) from 1998 to 2012, regions with values $\geq$ 50 W/m^2
977 (enclosed by thin gray line), and subdomains analyzed over the Indian Ocean (IO), western Pacific (WP), central
978 Pacific (CP), and Atlantic Ocean (AO) (green boxes).

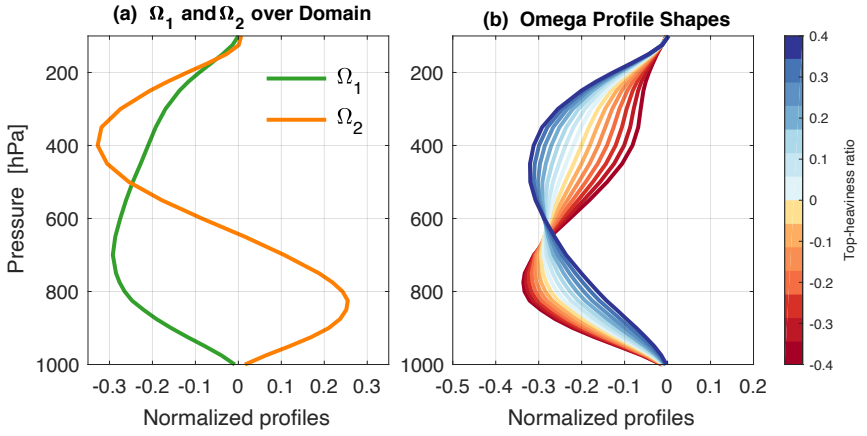

979 FIG. 2. (a): EOF1 and EOF2 of ω over the convergence regions enclosed by the gray line in Fig. 1; (b): The
980 shape of ω profiles with different top-heaviness ratios.

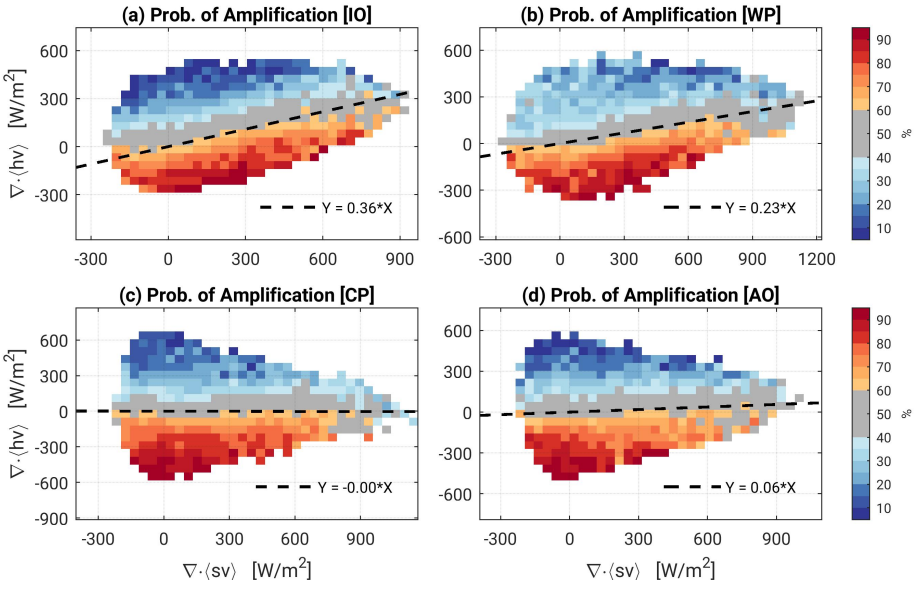

981 FIG. 3. Probabilities of precipitation amplification within bins of $\nabla \cdot \langle h\mathbf{v} \rangle$ and $\nabla \cdot \langle s\mathbf{v} \rangle$ over (a): IO, (b): WP,
982 (c): CP, and (d): AO, shown in Fig. 1 during JJA. Dashed-line slopes are $\widetilde{\gamma}$ over each basin, defined in Eq. (7).
983 Bins with <20 data points are omitted.

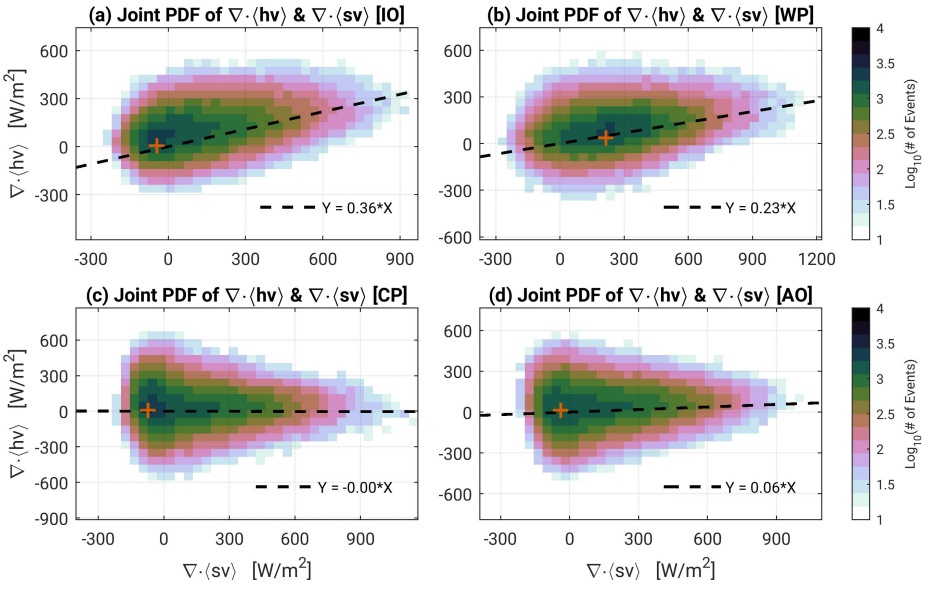

Fig. 4. Joint probability density functions (PDFs) of $\nabla \cdot \langle h\mathbf{v} \rangle$ and $\nabla \cdot \langle s\mathbf{v} \rangle$ over (a): IO, (b): WP, (c): CP, and (d): AO, with respective peaks at $[\nabla \cdot \langle s\mathbf{v} \rangle, \nabla \cdot \langle h\mathbf{v} \rangle] = [-44, 7]$, $[214, 38]$, $[-74, 11]$, and $[-39, 18]$ W/m^2 (orange crosses). Occurrences are binned as in Fig. 3.

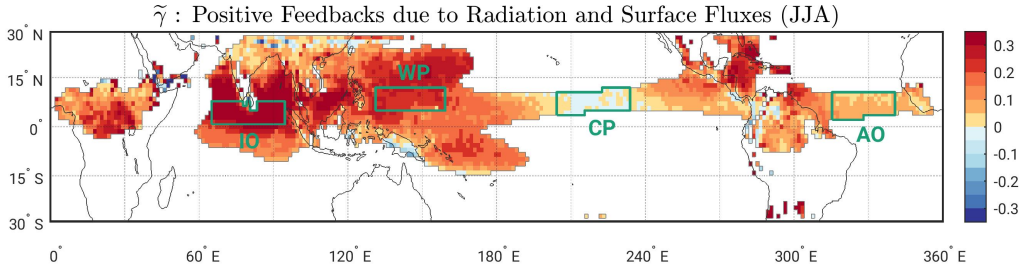

FIG. 5. Map of $\widetilde{\gamma}$ during JJA, defined following Eq. (7), shown where mean $\langle \omega \partial s/\partial p \rangle \geq 50$ W/m^2.

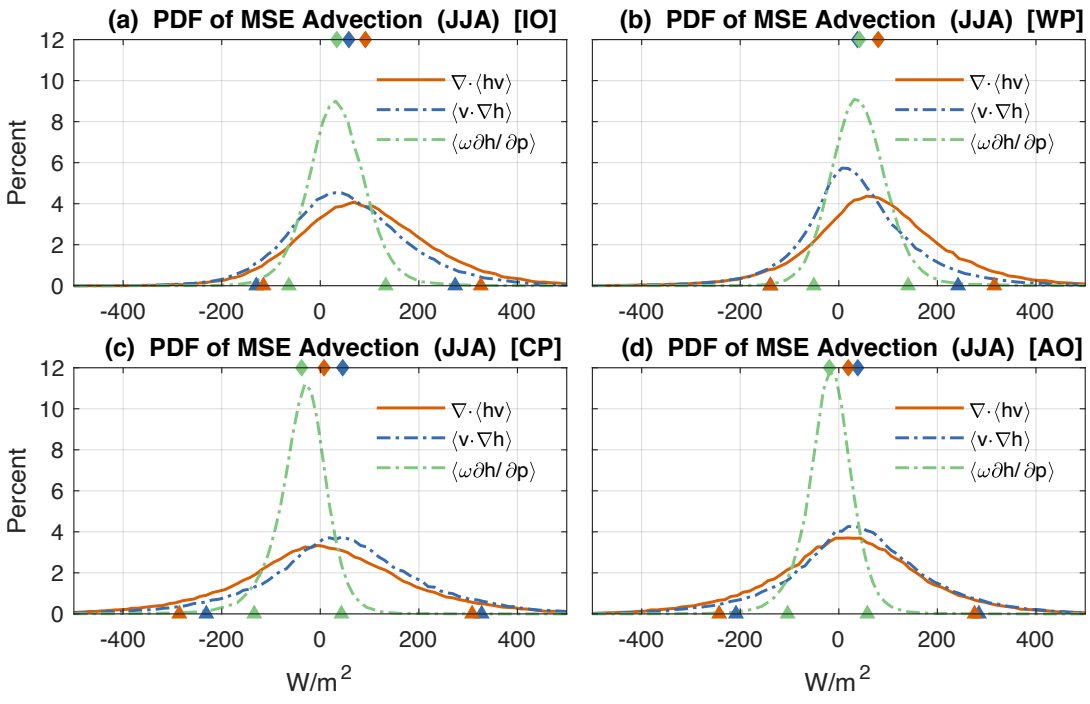

FIG. 6. Probability density functions (PDFs) of $\nabla \cdot \langle h\mathbf{v} \rangle$ (orange solid line), $\langle \mathbf{v} \cdot \nabla h \rangle$ (blue dash-dot line), and $\langle \omega \partial h / \partial p \rangle$ (green dash-dot line) over the four oceanic basins in JJA. The triangles on the bottom axis show the 5-percentile and 95-percentile of $\nabla \cdot \langle h\mathbf{v} \rangle$ (orange), $\langle \mathbf{v} \cdot \nabla h \rangle$ (blue), and $\langle \omega \partial h / \partial p \rangle$ (green); The diamonds on the top axis show the mean values with the same color arrangement.

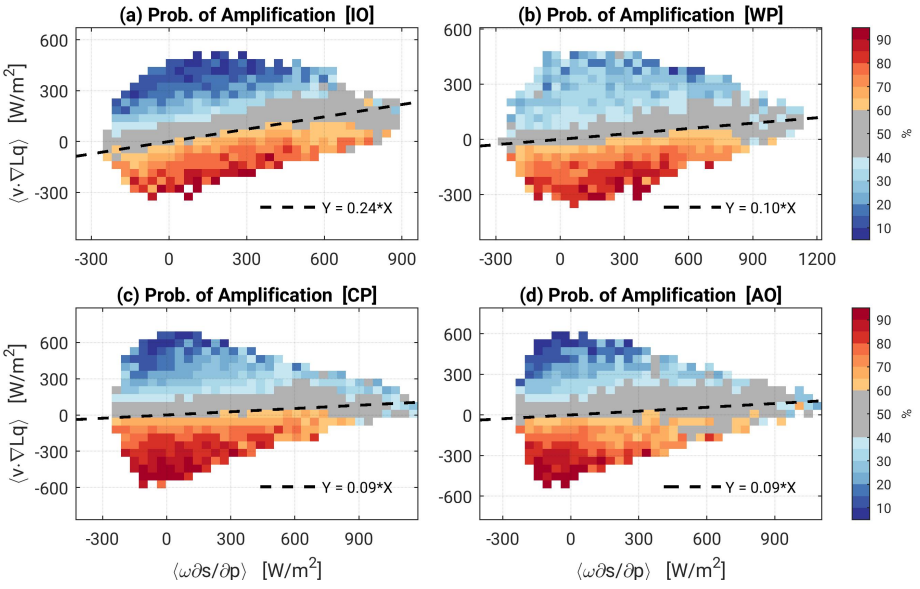

991 FIG. 7. As in Fig. 3, but the x- and y-axes are replaced with $\langle \omega \partial s/\partial p \rangle$ and $\langle \mathbf{v} \cdot \nabla Lq \rangle$, respectively. The dashed-
992 line slopes correspond to $\widetilde{\gamma} - \widetilde{\Gamma}_{\mathrm{v}}$ in Eq. (20), calculated with regression through the origin for each oceanic basin.
993 This figure is based on the hypothesis of Eq. (21).

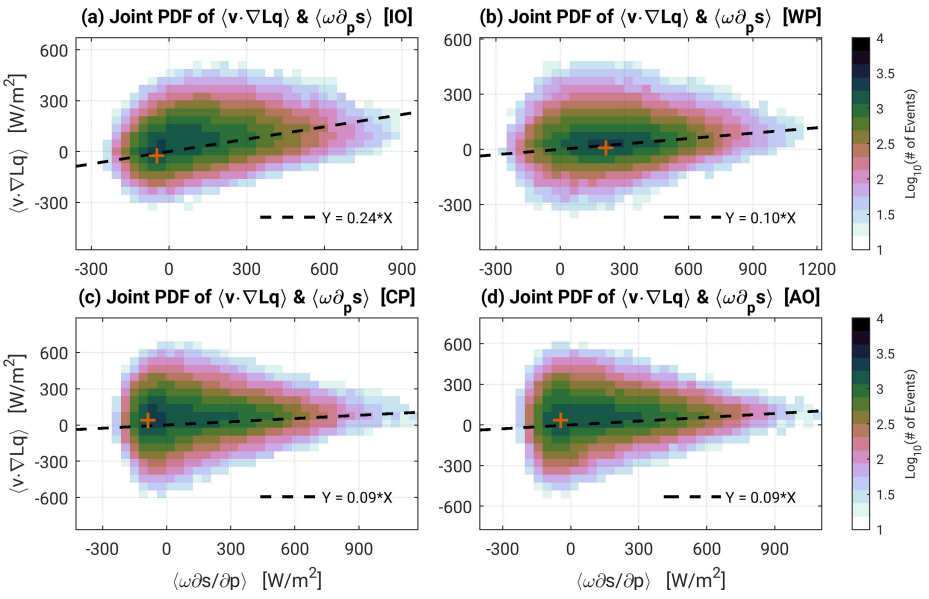

994 FIG. 8. As in Fig. 4, but for $\langle \mathbf{v} \cdot \nabla Lq \rangle$ and $\langle \omega \partial s / \partial p \rangle$. The numbers of occurrences were counted in the same
995 bins as in Fig. 7. The peaks of the distributions (orange crosses) for IO, WP, CP, and AO are, respectively, at
996 $[\langle \omega \partial s / \partial p \rangle, \langle \mathbf{v} \cdot \nabla Lq \rangle] = [-47, -23]$, $[213, 9]$, $[-89, 42]$, and $[-45, 38]$ (W/m^2).

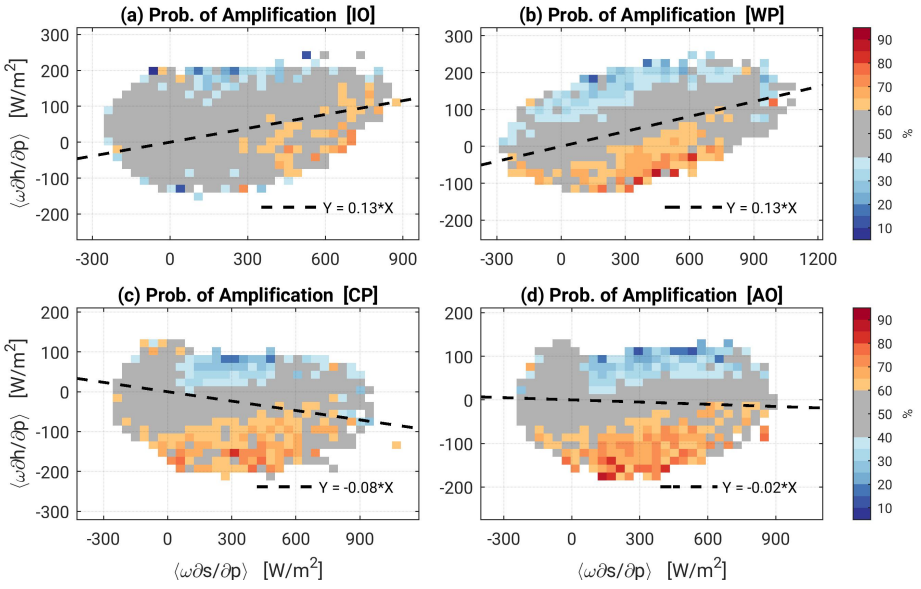

997 FIG. 9. As in Fig. 7, except the y-axis is replaced with $\langle \omega \partial h/\partial p \rangle$. The dashed-line slopes correspond to $\widetilde{\gamma} - \widetilde{\Gamma}_{\mathrm{h}}$
998 in Eq. (22), calculated with regression through the origin for each oceanic basin. This figure is based on the
999 hypothesis of Eq. (22).

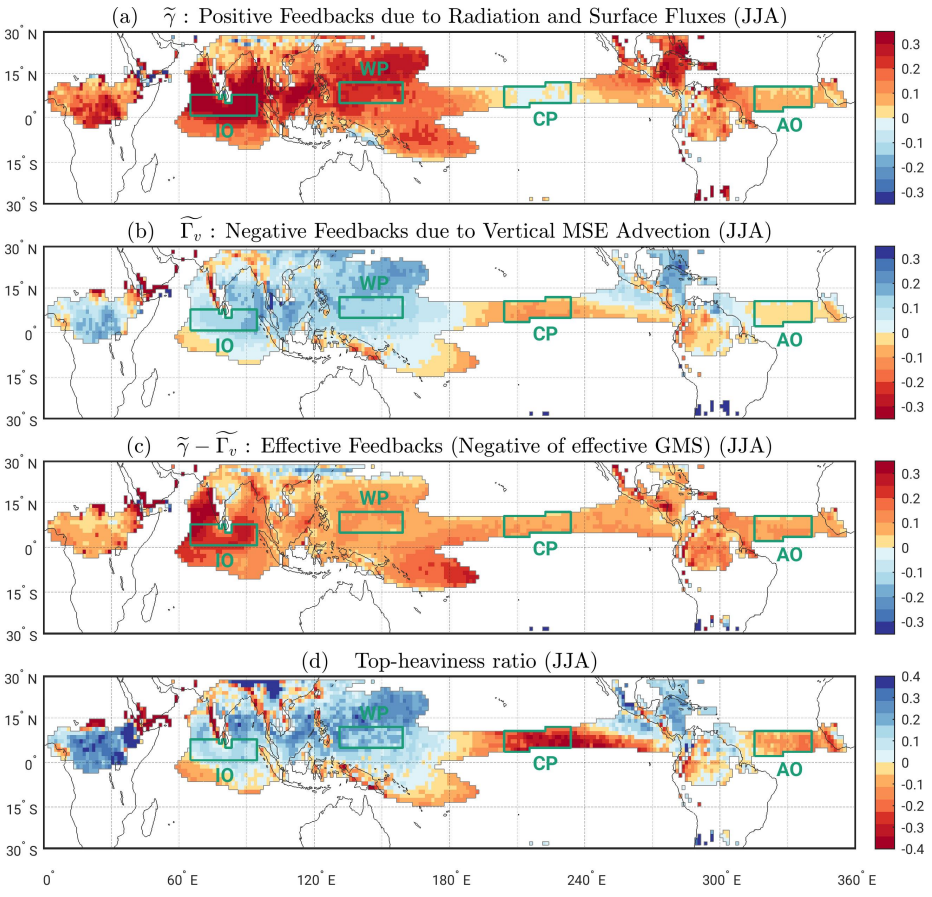

FIG. 10. (a): Identical to Fig. 5. Maps of (b) $\widetilde{\Gamma}_{\rm v}$ or vertical GMS, (c) $\widetilde{\gamma} - \widetilde{\Gamma}_{\rm v}$ or an effective feedback, equivalent to the negative of the effective GMS, and (d) the top-heaviness ratio $\widetilde{\tau}$, computed with Eq. (14). The color scale in panel (b) is flipped so that the red colors correspond to positive feedbacks. The color scale in panel (d) is the same as that in Fig. 2 (b). All panels are for JJA.

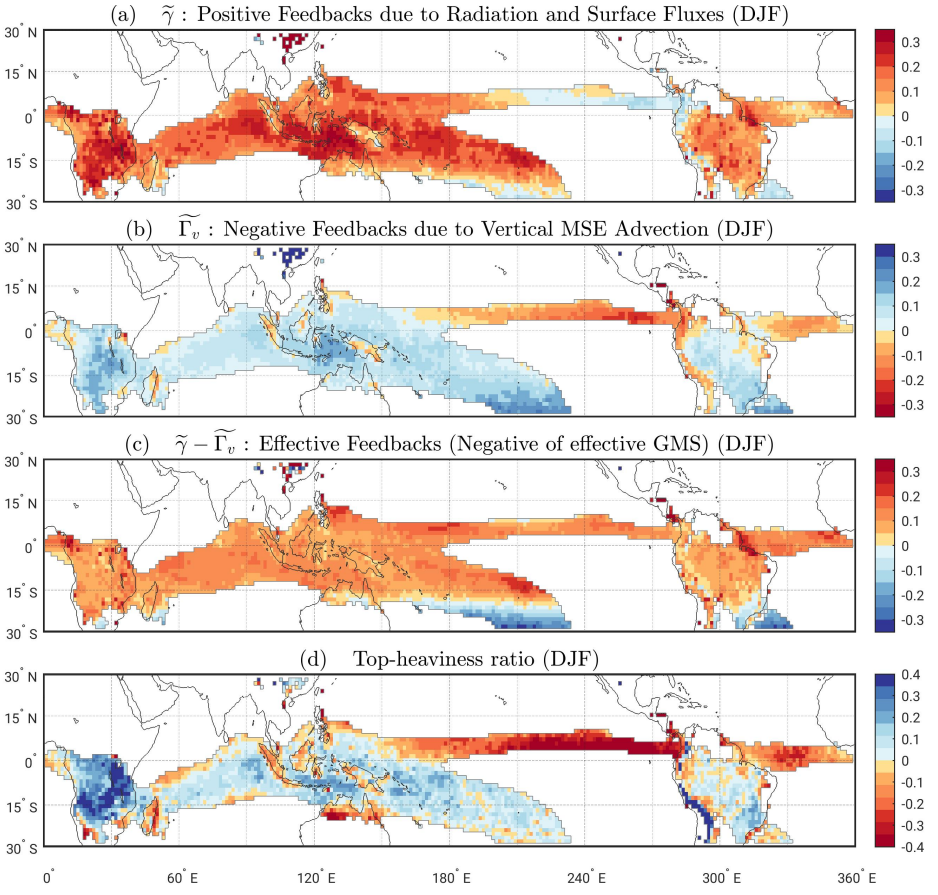

FIG. 11. As in Fig. 10, but for DJF, only over the regions with $\overline{\langle \omega \partial s/\partial p \rangle} \geq 50 \mathrm{W/m}^2$.

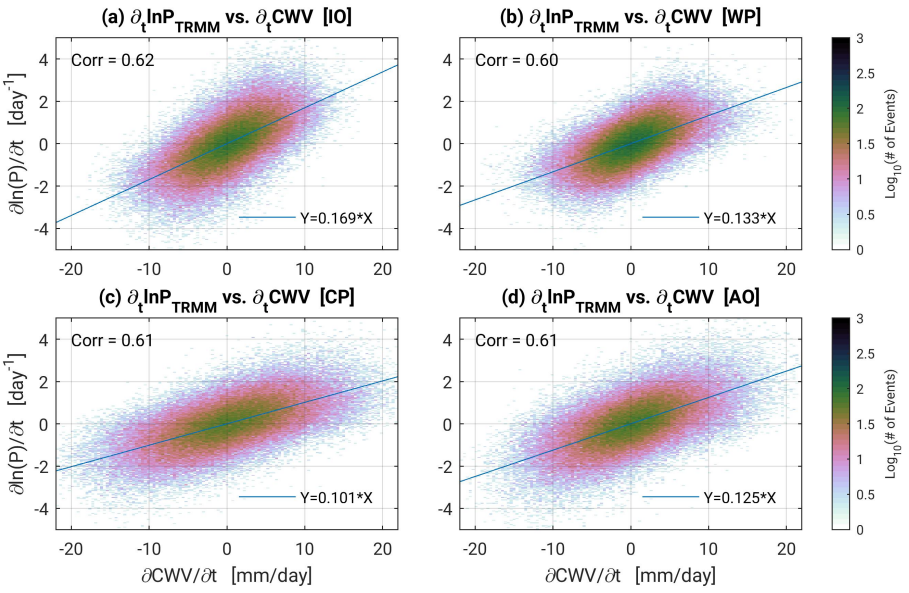

Fig. A1. Joint probability density functions of the tendency of $\ln P$ versus the tendency of $\langle q \rangle$ or CWV for (a) IO, (b) WP, (c) CP, and (d) AO during JJA. The colored shade represents the number of occurrences on the scale of $\log_{10}$. The numbers at the left corners represent correlation coefficients. The blue lines are calculated with the least squares method.